Astronomy & Astrophysics manuscript no. main
June 11, 2026
©ESO 2026

arXiv:2606.12076v1 [astro-ph.GA] 10 Jun 2026

X-ray luminosity function of Compton-thick AGN in the early Universe ($z \geq 3$)

Robustness and biases of the CTK population

A. Ruiz[1], E. Pouliasis[1], and I. Georgantopoulos[1]

IAASARS, National Observatory of Athens, Ioannou Metaxa and Vasileos Pavlou GR-15236, Athens, Greece
e-mail: ruizca@noa.gr

Received November 7th, 2025 ; Accepted June 8th, 2026

ABSTRACT

The population of Compton-thick (CTK) active galactic nuclei (AGN) represents a critical yet elusive phase in the growth of supermassive black holes (SMBHs). Constraining their abundance and evolution at high redshift is essential for understanding both SMBH growth and the origin of the cosmic X-ray background. We investigate the X-ray luminosity function (XLF) of CTK AGN at $z \geq 3$ using one of the largest available samples of X-ray-selected AGN at high redshift, containing 811 sources from *XMM-Newton* XXL-N and *Chandra* CCLS and CDF-S/N surveys. We first selected a subsample of ten high-probability CTK candidates, identified through Bayesian X-ray spectral fitting. Their multiwavelength properties are examined through spectral energy distribution modelling to assess the robustness of their CTK classification. For most sources, the inferred X-ray luminosities—and consequently their hydrogen column densities ($N_{\rm H}$)—appear overestimated when compared with their infrared (IR) luminosities. After updating the $N_{\rm H}$ posteriors with IR-informed priors, only three sources remain consistent with the CTK regime. To compute the XLF for the entire CTK AGN population, we used 24 µm photometry to estimate IR luminosities and update the X-ray posteriors for all the remaining sources. Incorporating IR priors systematically reduces the inferred CTK number densities, yielding a more conservative and physically consistent estimate of the X-ray luminosity and absorption functions. We find that CTK AGN constitute 17^{+12}_{-11}% of the total AGN population at $3 \leq z \leq 6$, consistent with results at lower redshifts. Our analysis reveals no statistically significant evolution in the CTK fraction up to $z \sim 6$, suggesting that the most heavily obscured accretion phase remains a persistent component of black hole growth throughout cosmic history. While the overall obscured AGN fraction ($N_{\rm H} > 10^{23}{\rm cm}^{-2}$) increases toward higher redshifts, the stable CTK fraction supports the interpretation that, at these epochs, the interstellar medium in typical host galaxies cannot produce CTK levels of obscuration.

Key words. Galaxies: active – X-rays: galaxies – Methods: data analysis – Methods: observational – Methods: statistical – early Universe

1. Introduction

Active galactic nuclei (AGN) are among the most luminous sources in the Universe, powered by accretion onto supermassive black holes (SMBHs) in their centres (Lynden-Bell 1969). These black holes have masses typically in the range $10^6 - 10^9 M_\odot$. Matter infalling towards the SMBH forms an accretion disc radiating in the extreme ultraviolet (UV), while X-rays are produced by inverse Compton scattering of these photons in a hot corona of electrons above the disc (e.g. Haardt & Maraschi 1991). The primary X-ray emission is often absorbed by gas and dust (Alexander & Hickox 2012; Brandt & Alexander 2015; Netzer 2015), historically interpreted as a toroidal structure (Antonucci & Miller 1985), though infrared (IR) and sub-mm imaging reveals a more complex morphology (Hönig et al. 2012; García-Burillo et al. 2016).

Because X-rays penetrate large column densities, they offer a powerful means of tracing AGN activity across cosmic time. Observations with *Chandra* and *XMM-Newton* have mapped the accretion history of SMBHs up to $z \sim 3$ (e.g. Ueda et al. 2014; Aird et al. 2015b; Buchner et al. 2015; Miyaji et al. 2015; Fotopoulou et al. 2016; Georgakakis et al. 2017). At higher redshifts ($z = 3 - 6$), the AGN luminosity function has been explored by Georgakakis et al. (2015), Vito et al. (2018), and Pouliasis et al. (2024), who showed that AGN were more abundant at earlier epochs, with the number density peak depending on luminosity. These studies also established that obscuration increases with redshift: the fraction of obscured AGN with $\log N_{\rm H} > 23$ rises from $\sim$ 50% at $z \approx 1$ (Signorini et al. 2023; Vijarnwannaluk et al. 2024) to $\sim$ 75% at $z \geq 3$ (Vito et al. 2018; Pouliasis et al. 2024). Lower column densities of the order of $\log N_{\rm H} \sim 22$ cannot be easily constrained at high redshifts as the obscuration low energy turnover is redshifted out of the *XMM-Newton* and *Chandra* bandpass. The increase of the column density with redshift likely reflects the higher gas and dust content of early galaxies, as supported by ALMA observations (Scoville et al. 2017; Gilli et al. 2022).

For column densities above $\log N_{\rm H} \approx 24$, gas becomes optically thick to Compton scattering, defining the Compton-thick (CTK) regime. CTK AGN are key to understanding SMBH growth, AGN–galaxy co-evolution, and the origin of the cosmic X-ray background (Comastri et al. 1995; Gilli et al. 2007; Akylas et al. 2012; Ananna et al. 2019). Hard X-ray (14-195 keV) surveys with *Swift*-BAT (Barthelmy et al. 2005) have provided robust constraints in the local Universe ($z \lesssim 0.1$), yielding observed CTK fractions of $\lesssim$ 20% (Burlon et al.

Table 1: Compton-thick candidates selected from the Pouliasis et al. (2024) sample of high-redshift AGN. Quoted uncertainties (or lower limits) correspond to 90% highest probability density intervals.

Source	Survey	R.A.	Dec.	Redshift[a]	log L_X[b]	log N_H[c]	Prob. CTK
hz414292	XXL-N	02:19:01.4	-05:40:11.10	3.24†	$46.2^{+0.3}_{-1.1}$	> 23.5	0.70
hz434324	XXL-N	02:22:16.4	-04:59:33.26	3.16	$45.8^{+0.3}_{-1.1}$	> 23.6	0.84
cdfs101	CDF-S	03:32:01.6	-27:44:02.88	3.47	$44.7^{+0.3}_{-0.3}$	> 24.4	0.95
cdfs337	CDF-S	03:32:18.8	-27:51:35.29	**3.6600**	$44.7^{+0.4}_{-0.3}$	$24.16^{+0.53}_{-0.33}$	0.93
cdfs657	CDF-S	03:32:35.2	-27:52:15.30	3.47	$44.1^{+0.5}_{-0.2}$	$24.04^{+0.85}_{-0.23}$	0.84
lid_1278	CCLS	09:58:38.2	+01:35:46.76	3.01	$45.9^{+0.4}_{-1.0}$	> 23.6	0.87
cid_965	CCLS	10:00:36.5	+02:18:28.14	**3.1780**	$45.4^{+0.4}_{-0.5}$	$24.16^{+1.54}_{-0.34}$	0.86
lid_439	CCLS	10:01:59.0	+02:48:02.62	2.93	$45.9^{+0.3}_{-1.0}$	$24.56^{+1.37}_{-0.94}$	0.85
cdfn158	CDF-N	12:36:19.9	+62:19:10.20	3.19	$45.2^{+0.2}_{-0.2}$	> 24.5	0.97
cdfn257	CDF-N	12:36:36.9	+62:13:20.10	**2.95**†	$44.4^{+0.2}_{-1.3}$	$23.5^{+2.0}_{-0.3}$	0.72

Notes. (a) Bold values correspond to spectroscopic redshifts; (b) Decimal logarithm of the 2-10 keV luminosity, absorption corrected, in erg s^{-1}; (c) Decimal logarithm of the hydrogen column density, in units of cm^{-2}. † Updated redshift after visual inspection of the optical and IR counterparts.

2011; Akylas et al. 2016; Georgantopoulos & Akylas 2019; Torres-Albà et al. 2021) and intrinsic fractions of $\sim 20-30\%$ after flux bias corrections (Ricci et al. 2015; Akylas et al. 2024; Annuar et al. 2025).

The broad energy range of NuSTAR detectors (8—79 keV) makes it a powerful tool for the study of CTK-AGN albeit its sensitivity limits its ability to study obscured AGN in the high redshift ($z > 3$) regime. Recent studies based on *NuSTAR* observations yield similar results for the fraction of CTK AGN in the local Universe (Boorman et al. 2025; Georgantopoulos et al. 2025). Ananna et al. (2019) reported a fraction of CTK-AGN in the local universe ($z \approx 0.1$) that can reach up $50 \pm 9\%$ provided that extremely obscured sources with $\log N_H > 25$ are taken into account. This result is derived from a population synthesis model fitting the observed Cosmic X-ray Background in the 0.5–100 keV energy range.

Beyond the local Universe, CTK AGN have been systematically identified up to about $z = 3$ using *Chandra* and *XMM-Newton* (e.g. Georgantopoulos et al. 2013; Brightman et al. 2014; Buchner et al. 2015; Lanzuisi et al. 2015, 2018; Georgakakis et al. 2017; Laloux et al. 2023), but their fraction and evolution remain uncertain. Buchner et al. (2015) reported a CTK fraction of $43\pm10\%$ with no clear redshift dependence, whereas Lanzuisi et al. (2018) found evidence for strong evolution, reaching $\sim 45\%$ at $z > 2$. More recently, Laloux et al. (2023) introduced a method combining X-ray spectra with IR priors, enabling the rejection of spurious CTK classifications. Their results are consistent with the local BAT estimates and with no significant evolution of the CTK fraction.

In this work, we revisit the CTK AGN luminosity function at $z > 3$ using the *XMM-Newton* XXL-N, *Chandra* COSMOS Legacy, and *Chandra* Deep Field (South and North) surveys. Building on Pouliasis et al. (2024), who derived the X-ray luminosity and absorption functions (XLAF) for $z = 3-6$, we focus here on the CTK regime ($N_H \geq 10^{24}$ cm^{-2}). We re-evaluate CTK candidates through multiwavelength analysis and compare their intrinsic X-ray and IR luminosities to assess the reliability of their CTK classification. These effects are taken into account to calculate the luminosity function for CTK AGN in a more conservative and physically consistent way.

The paper is organised as follows: Sect. 2 describes the initial high-redshift sample and CTK candidate selection; Sect. 3 presents the analysis and results; Sect. 4 discusses our findings; and Sect. 5 summarises our conclusions. Throughout this paper, we adopt a ΛCDM cosmology with $H_0 = 70\,km\,s^{-1}\,Mpc^{-1}$, $\Omega_m = 0.3$ and $\Omega_\Lambda = 0.7$ (Komatsu et al. 2009).

2. Data and sample selection

In Pouliasis et al. (2024) we presented one of the largest samples of high-redshift ($z \geq 3$), X-ray-selected (0.5-2 keV band) AGN, comprising 811 sources. The sample was assembled using data from three major X-ray surveys: *Chandra* Deep Field South and North (CDF-S/N; Luo et al. 2017; Xue et al. 2016), *Chandra* COSMOS Legacy Survey (CCLS; Civano et al. 2016), and the northern field of the *XMM-Newton* XXL survey (XXL-N; Pierre et al. 2016). The combination of survey depths and sky areas provides broad coverage in X-ray luminosity, redshift, and absorption column density.

The high optical identification rates of these surveys allow the construction of a highly complete sample in terms of distance information, based either on spectroscopic redshifts, when available, or probabilistic photometric redshifts. For the *Chandra* surveys, Pouliasis et al. (2024) adopted photometric redshifts from the literature (Vito et al. 2018; Marchesi et al. 2016), while for XXL-N, new photometric redshifts were derived using deeper optical imaging from the Hyper Suprime-Cam (HSC) survey (Miyazaki et al. 2018). The final Pouliasis et al. (2024) sample includes all sources with spectroscopic redshifts $z \geq 3$ (191 sources) and those with photometric redshifts having a probability greater than 20% of being at $z \geq 3$ (620 sources). When weighting the photometric-redshift sources by their high-redshift probabilities, the effective total number of sources is 631.2.

X-ray spectra for all sources were extracted using the standard tools for the corresponding missions, CIAO (v4.13) for *Chandra* and SAS (v19) for *XMM-Newton*(See Sect. 3.1 of Pouliasis et al. 2024, for details) and modelled using the Bayesian X-ray Analysis framework (Buchner et al. 2014; Buchner 2021) in combination with the `UXClumpy` torus model (Buchner et al. 2019) to estimate intrinsic X-ray properties (See Sect. 3.2 of Pouliasis et al. 2024, for details on the X-ray spectral modelling) such as absorption-corrected 2–10 keV luminosities (L_X) and hydrogen column densities (N_H).[1] For each source, this procedure yields a posterior probability distribution in redshift, luminosity, and absorption, $P(z, \log L_X, \log N_H|X)$.

[1] Throughout this paper we always use cgs units for L_X (erg s^{-1}) and N_H (cm^{-2}). When quoting logarithmic values for this quantities, the corresponding cgs units are implied.

Pouliasis et al. (2024) used these posteriors to derive a parametric model for the joint X-ray luminosity and absorption function of AGN (see Appendix A for a detailed description of the methodology employed) with $3 \leq z \leq 6$ and $20 \leq \log N_{\rm H} \leq 26$, focusing primarily on the unabsorbed and Compton-thin ($22 \leq \log N_{\rm H} \leq 24$) regime. In the present work, we extend this analysis to the CTK domain, aiming to assess the reliability of X-ray spectral constraints for potential CTK candidates. To this end, we select a subsample of sources with a high probability of being CTK, based solely on their X-ray properties, as described in Sect. 2.1 below.

2.1. Sample of CTK AGN

We identified compelling candidates for high-redshift CTK AGN within the Pouliasis et al. (2024) sample. Using the posterior probability distributions derived from the X-ray spectral analysis, we computed the marginalised one-dimensional probabilities for z and $\log N_{\rm H}$ and selected sources with a probability exceeding 80% of having $z > 2.5$ and $\log N_{\rm H} > 24$. Twelve sources satisfied these criteria.

We then visually inspected the optical and IR images of these twelve sources to confirm the correct counterparts. Two XXL-N sources (hz428174 and hz414292) were found to have incorrect associations; we recalculated their photometric redshifts using the corrected photometry, after which only hz414292 remained in the sample. One CDF-S source (cdfs412) had an erroneous spectroscopic redshift; its photometric redshift falls below our selection threshold, and it was therefore excluded from the sample. One source in CDF-N (cdfn257) has a JWST spectrum with $z = 2.95$, consistent with our initial photometric redshift estimate. We re-ran the X-ray spectral analysis for all sources with updated redshifts. The final sample comprises ten sources, listed in Table 1. Figure 1 shows the 2–10 keV luminosity versus the hydrogen column density for the full Pouliasis et al. (2024) sample, highlighting the selected CTK candidates.

2.2. Multi-wavelength counterparts

We compiled multiwavelength photometric data, spanning from the optical to mid-infrared (MIR) regime, for our sample of CTK AGN using publicly available catalogues from the literature.

For sources in the XXL-N field, we adopted the photometric catalogue of Pouliasis et al. (2024), which incorporates deeper imaging from recent public data releases and updates the earlier compilation of Pouliasis et al. (2022). This catalogue provides optical photometry from HSC (*g, r, i, z, Y* bands; Miyazaki et al. 2018), complemented by *u*-band data from the Canada France Hawaii Telescope (CFHT; Sawicki et al. 2019), and near-infrared (NIR) measurements (*J, H, Ks*) from UKIDSS (DXS/UDS; Lawrence et al. 2007) and from several VISTA surveys: VHS (Vista Hemisphere Survey, McMahon et al. 2013), VIKING (VISTA Kilo-degree Infrared Galaxy, Edge et al. 2013) and VIDEO (VISTA Deep Extragalactic Observations, Jarvis et al. 2013). We further supplemented this dataset with MIR photometry from the *Spitzer* Enhanced Imaging Products (SEIP; IRSA & SSC 2020) catalogue, including all four IRAC bands (3.6, 4.5, 5.8, and 8.0 μm) and the MIPS 24 μm band.

For sources in the CCLS field, we used the COSMOS2020 catalogue (Weaver et al. 2022), which combines optical data from HSC (*g, r, i, z, Y*) and CFHT (*u*), NIR data from VISTA (*Y, J, Ks*), and MIR photometry from *Spitzer*–IRAC. We complemented this with *Spitzer*-MIPS 24 μm fluxes from the HELP catalogues (Shirley et al. 2021).

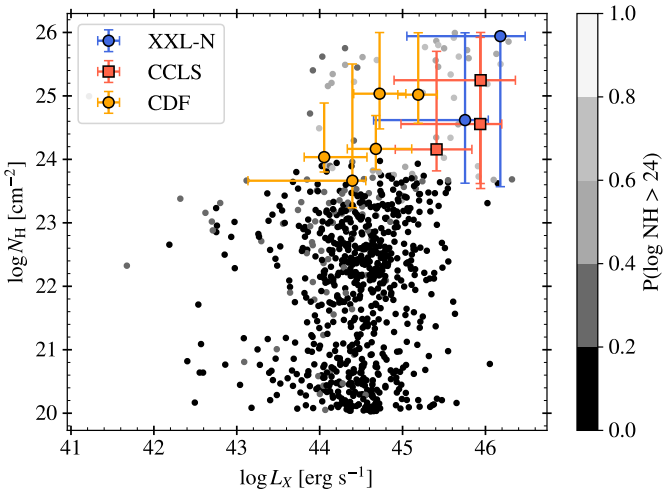


Fig. 1: Intrinsic X-ray luminosity in the 2–10 keV band versus hydrogen column density. Small circles show the full sample from Pouliasis et al. (2024), shaded by the probability of being CTK. Large circles mark our selection of CTK candidates, as described in Sect. 2.1, colour-coded according to their parent X-ray survey (yellow: CDF, red: CCLS, blue: XXL-N). For clarity, error bars (indicating 90% credible intervals) are shown only for the CTK candidates.

For the CDF-S field, photometric data were obtained from the ZFOURGE catalogue (Straatman et al. 2016), which includes optical imaging from VLT–VIMOS (*U* band) and HST–ACS (F435W, F606W, F775W, F850LP), complemented by NIR observations from Magellan–FourStar (*J, Hs, Hl*) and MIR data from *Spitzer* (3.6, 4.5, 5.8, 8.0, and 24 μm).

In the CDF-N field, we adopted the photometric compilation of Xue et al. (2016), who identified optical counterparts to X-ray sources using the HST GOODS-N (Giavalisco et al. 2004) and CANDELS (Grogin et al. 2011; Koekemoer et al. 2011) datasets. This catalogue includes optical and NIR photometry from HST–ACS (F606W) and HST–WFC3 (F125W, F140W, F160W), together with MIR measurements from *Spitzer* covering all IRAC bands and the 24 μm MIPS channel (Ashby et al. 2013).

3. Data Analysis

3.1. Spectral energy distributions of the CTK candidates

We investigated additional evidence supporting the CTK nature of our selected sources by analysing their multiwavelength properties. CTK AGN are expected to exhibit characteristics typical of Type 2 AGN, where the optical continuum is dominated by the stellar emission of the host galaxy due to the obscuration of the accretion disc by the AGN torus. In contrast, strong thermal emission from the torus is expected in the IR, particularly in the mid-IR, where it can dominate the overall energy output (Nenkova et al. 2008a,b; Sajina et al. 2022).

To explore this, we used the photometric data presented in Sect. 2.2 to construct the spectral energy distributions (SEDs) of our CTK candidates. These SEDs were modelled using `CIGALE` (Code Investigating GALaxy Emission; Boquien et al. 2019), a Python-based SED fitting tool designed to disentangle galaxy

Table 2: Best-fit model parameters from CIGALE SED fitting. Errors and upper-limits correspond to 1-σ confidence intervals.

Source [(a)]	Survey	Redshift [(b)]	red.χ^2	AGN fraction		Inclination		$\log L_{6\,\mu m}^{AGN}$ [(c)]		$\log N_H^{IR}$ [(d)]
				bayes	best	bayes	best	bayes	best	
hz414292	XXL-N	3.24	2.5	< 0.37	0.1	52 ± 8	50	$45.3^{+0.2}_{-0.5}$	45.2	$23.7^{+0.7}_{-0.6}$
hz434324	XXL-N	3.16	1.5	< 0.40	0.2	64 ± 22	30	< 44.8	44.0	$23.5^{+0.5}_{-1.8}$
cdfs101	CDF-S	3.47	0.5	< 0.37	0.8	63 ± 18	50	$44.5^{+0.3}_{-0.8}$	44.8	24.9 ± 1.0
cdfs337	CDF-S	**3.6600**	3.8	0.54 ± 0.19	0.5	75 ± 14	50	$45.1^{+0.1}_{-0.2}$	44.9	24.2 ± 0.3
cdfs657	CDF-S	3.47	0.8	< 0.30	0.3	71 ± 19	70	< 44.1	43.9	24.0 ± 0.2
lid_1278	CCLS	3.01	2.0	0.51 ± 0.18	0.7	73 ± 11	70	$45.0^{+0.1}_{-0.2}$	45.2	$23.3^{+0.4}_{-0.2}$
cid_965	CCLS	**3.1780**	0.4	0.73 ± 0.10	0.8	50 ± 1	50	$45.41^{+0.04}_{-0.05}$	45.4	$24.2^{+0.2}_{-0.5}$
lid_439	CCLS	2.93	4.8	0.63 ± 0.17	0.5	76 ± 12	70	$44.7^{+0.1}_{-0.2}$	44.8	$23.6^{+0.13}_{-0.6}$
cdfn158	CDF-N	3.19	2.4	0.35 ± 0.18	0.3	50 ± 4	50	$45.5^{+0.1}_{-0.2}$	45.5	$25.0^{+1.0}_{-0.6}$
cdfn257	CDF-N	**2.95**	0.5	< 0.3	0.4	67 ± 19	50	$44.1^{+0.3}_{-0.8}$	44.2	$24.5^{+1.5}_{-0.7}$

Notes. (a) Sources that remain high likelihood CTK ($P(\log N_H > 24) > 0.8$ after our SED analysis showed in boldface; (b) Bold values correspond to spectroscopic redshifts; (c) Decimal logarithm of the luminosity of the AGN component at 6 µm in C.G.S. units; (d) Decimal logarithm of the $N_H$estimated with the IR-updated posteriors, following the method presented in Sect. 3.2.

and AGN emission components and derive their respective physical properties.

In summary, we employed the stellar synthesis population models of Bruzual & Charlot (2003), assuming a Salpeter (1955) initial mass function and a fixed metallicity of $Z = 0.02$. The star formation history follows a delayed model of the form SFR $\propto t \times e^{-t/\tau}$, incorporating a short starburst phase capped at 50 Myr. Dust emission was modelled using the templates of Dale et al. (2014), excluding any AGN contribution, while dust attenuation was treated using the extinction law of Charlot & Fall (2000). For the AGN component, we adopted the SKIRTOR model (Stalevski et al. 2012, 2016). The full list of modules and parameters used in our analysis is provided in Table C.1. This setup allowed us to fit the SEDs using a grid comprising over 29 million models.

The results of our SED fitting are summarized in Table 2. We report three key parameters relevant to our analysis: the inclination angle of the AGN torus, the AGN fractional contribution to the total IR emission, and the AGN luminosity at 6 µm. For each parameter, we provide two estimates: "best" refers to the values obtained from the model with the lowest χ^2 in the model grid explored by CIGALE, while "bayes" corresponds to the Bayesian estimate (i.e. the probability-weighted mean and standard deviation across all models).[2] As an example, Fig. 2 shows the best-fit SED model obtained by CIGALE for source lid_1278.

Our results are consistent with the presence of heavily obscured AGN. The high torus inclination angles indicate that the accretion disc emission is hidden in the optical regime. Although the Bayesian estimates for the AGN fraction are consistent with zero for some sources, visual inspection of the best-fitting SED models clearly shows that an AGN component is required to reproduce the observed 24 µm emission. The host-galaxy component alone cannot account for such high infrared fluxes, as also indicated by the non-zero "best" AGN fractions reported in Table 2. This is clearly illustrated in Fig. 2, where the optical part of the SED is dominated by the host galaxy (grey dotted line), whereas the rest-frame $\sim 3 - 30$ µm range is clearly dominated by the AGN component (red dashed line).

Although the overall SED shapes support the CTK scenario, they do not, by themselves, provide strong constraints on the column density of these sources. In Sect. 3.2 below, we explore how the AGN luminosity at 6 µm, derived from our SED analysis, can be used to further investigate this aspect.

[2] If the "bayes" value is consistent with zero, we quote the 1σ upper-limit.

3.2. Constraining the X-ray absorption via the $L_X - L_{6\,\mu m}$ correlation

A well-established correlation exists between AGN emission in the X-ray and MIR regimes, particularly between the rest-frame 2–10 keV and 6 µm luminosities (e.g. Mateos et al. 2015; Stern 2015; Chen et al. 2017; Toba et al. 2019). This correlation arises from the shared origin of both emissions: UV photons from the accretion disc serve as seed photons for Compton up-scattering in the X-ray corona, as well as for the thermal reprocessing by the circumnuclear dusty torus, which re-emits in the MIR. Owing to its robustness, this correlation has been used to identify heavily obscured AGN (Alexander et al. 2008; Georgantopoulos et al. 2011; Severgnini et al. 2012; Carroll et al. 2021), and more recently, to place constraints on the line-of-sight N_H via X-ray spectral modelling (Laloux et al. 2023).

In the left panel of Fig. 3, we present the rest-frame 2–10 keV luminosities derived from our X-ray spectral fits as a function of the rest-frame 6 µm luminosities obtained through SED modelling (Sect. 3.1) for the CTK candidates in our sample (coloured circles). For reference, we include a comparison sample of X-ray selected AGN from the CCLS (black dots; Laloux et al. 2023). The distribution of our sources reveals a systematic offset above the Stern (2015) correlation (black dashed line), with the XXL-N and most CCLS sources lying beyond the 2σ dispersion (gray dashed lines) derived from the Laloux et al. (2023) sample.

This discrepancy is further illustrated in Fig. 2, where we show the observed 6 µm flux inferred from the X-ray luminosities using the Stern (2015) relation (red cross). The expected IR flux is several orders of magnitude higher than what is predicted from our SED modelling, suggesting a significant overestimation of the X-ray luminosity. The availability of *Spitzer*-MIPS 24 µm imaging data for all CTK candidates provides a strong constraint on the rest-frame 6 µm emission at the redshift range of our sources, lending confidence to the reliability of the SED-derived IR luminosities.

The most plausible interpretation for the discrepancy is an overestimation of L_X, driven by uncertainties in N_H. Inspection of the N_H posterior distributions (lower right panels of Figs. B.1-

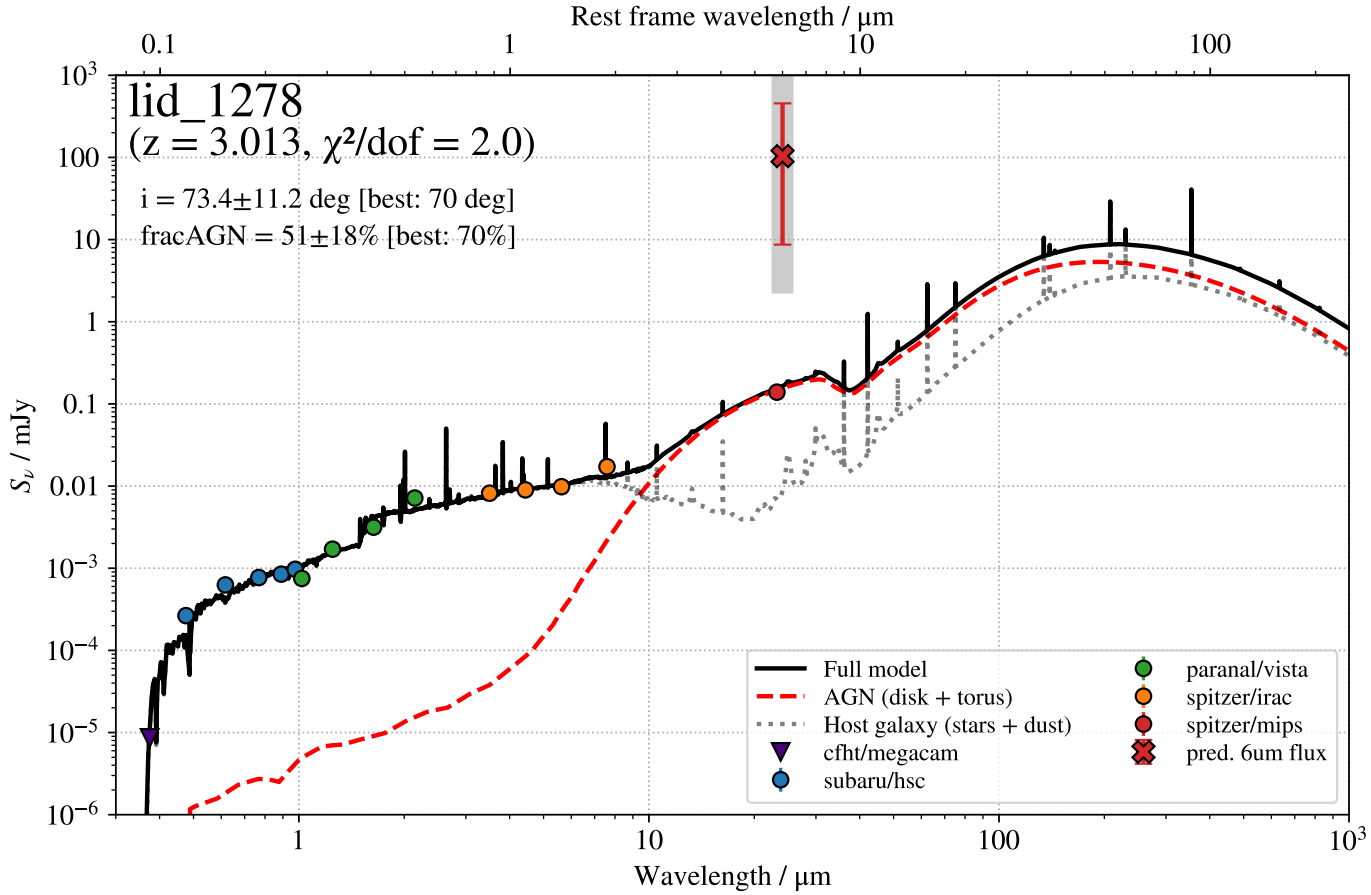


Fig. 2: Spectral energy distribution of source lid_1278 (z = 3.013), one of the CTK AGN candidates in our sample. The colour-coded symbols show the observed photometry from CFHT-MegaCam (purple), Subaru-HSC (blue), VISTA (green), *Spitzer*-IRAC (orange), and *Spitzer*-MIPS (red). The solid black line indicates the best-fitting total model from `CIGALE`, decomposed into the AGN (disc + torus; red dashed line) and host-galaxy (stars + dust; grey dotted line) components. The predicted 6 μm flux derived from the X-ray luminosity is also shown (red cross). The best-fitting parameters are reported in the legend, including inclination angle and AGN fractional contribution.

B.2) reveals that they are frequently broad or exhibit bimodal behaviour, with non-negligible posterior weight extending below the CTK threshold.

Figure 4 illustrates the joint posterior distribution in the $\log N_{\rm H} - \log L_{6\,\mu{\rm m}}$ plane (blue shaded region) for one of our CTK candidates, where $L_{6\,\mu{\rm m}}$ is computed from the $L_{\rm X}$ posterior using the Stern (2015) relation. The distribution is characteristically bimodal, with a primary peak at high $N_{\rm H}$ and high $L_{6\,\mu{\rm m}}$, and a secondary peak at lower $N_{\rm H}$ and correspondingly lower luminosity. Notably, the low-$N_{\rm H}$ solution aligns well with the SED-inferred $L_{6\,\mu{\rm m}}$ value (black dashed line and gray shaded region), suggesting that the CTK classification may be driven by poorly constrained or degenerate $N_{\rm H}$ estimates rather than robust spectral evidence.

Laloux et al. (2023) demonstrated that the degeneracy in the $\log N_{\rm H} - \log L_{\rm X}$ parameter space, commonly encountered in X-ray spectral fitting in the low-count regime, can be significantly reduced by incorporating IR luminosity constraints. In their approach, IR data are used to inform the X-ray spectral analysis through priors on the intrinsic X-ray luminosity, assuming a given $L_{\rm X} - L_{6\,\mu{\rm m}}$ correlation.

Following the same principle, we incorporate the constraints derived from our SED fitting into the X-ray analysis without re-performing the full spectral fit. Instead, we update the posterior probability distributions obtained with BXA using Bayes' theorem:

$$P(z, \log L_{\rm X}, \log N_{\rm H}|X, IR) \propto P(z, \log L_{\rm X}, \log N_{\rm H}|X) \times \mathcal{N}(\log L_{\rm X}|\mu, \sigma^2), \quad (1)$$

where $P(z, \log L_{\rm X}, \log N_{\rm H}|X)$ is the original posterior distribution from the X-ray-only analysis, and $\mathcal{N}$ is a Gaussian prior on $\log L_{\rm X}$ centred at the X-ray luminosity inferred from the SED-derived $L_{6\,\mu{\rm m}}$ (assuming the Stern 2015 correlation). The standard deviation σ of the prior is set to match the intrinsic scatter of the $L_{\rm X} - L_{6\,\mu{\rm m}}$ relation measured in the Laloux et al. (2023) sample. The updated posterior, $P(z, \log L_{\rm X}, \log N_{\rm H}|X, IR)$, incorporates the additional IR constraint. This method is illustrated in Fig. 4, where the red dotted region represents the IR-informed posterior distribution.

We applied this approach to all CTK candidates in our sample. The right panel of Fig. 3 compares the updated $L_{\rm X}$ values against the SED-inferred 6 μm luminosities. After incorporating the IR priors, the sources fall closer to the expected relation from Stern (2015), although a slight systematic overestimation of $L_{\rm X}$ persists. Importantly, the updated posteriors have a significant impact on the inferred $N_{\rm H}$ values. Figure 6 shows a comparison of the posterior probabilities of each source being CTK, obtained using the X-ray-only (grey bars) and IR-informed (red

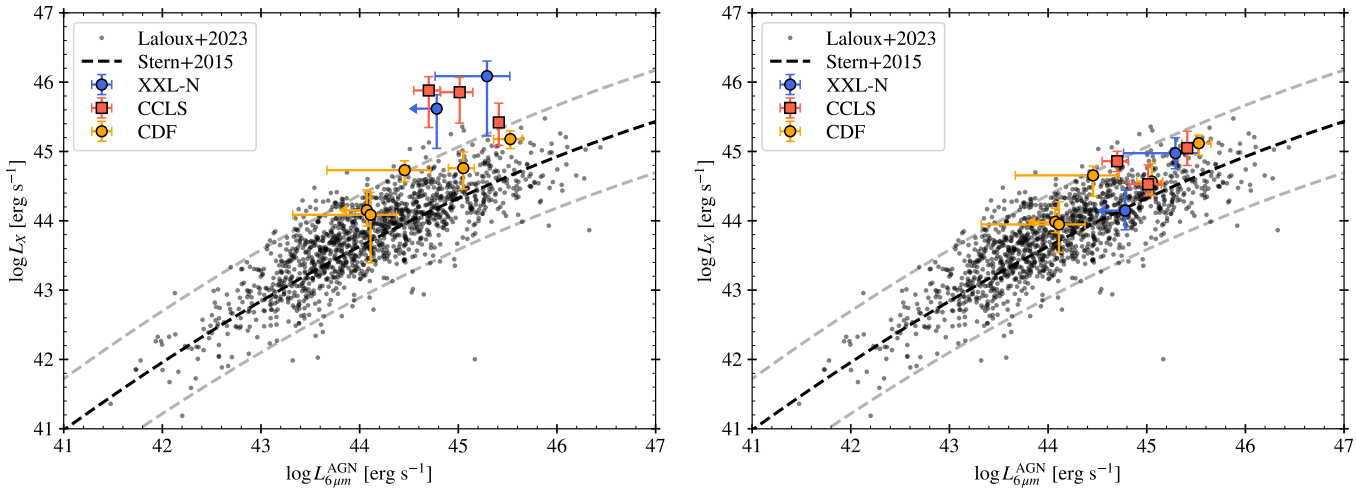


Fig. 3: Intrinsic X-ray luminosity in the 2–10 keV band versus the monochromatic 6 µm luminosity of the AGN component. The results for our CTK sample are shown before (left panel) and after (right panel) applying the infrared luminosity prior, as described in Sect. 3.2. Grey dots represent the X-ray–selected AGN sample from Laloux et al. (2023) in the CCLS field. Large circles indicate our final CTK candidates, colour-coded by their parent X-ray survey (yellow: CDF; red: CCLS; blue: XXL-N). The black dashed line marks the $L_X - L_{6\,\mu m}$ relation from Stern (2015), while the grey dashed lines denote the 2σ dispersion of the Laloux et al. (2023) sample with respect to that relation.

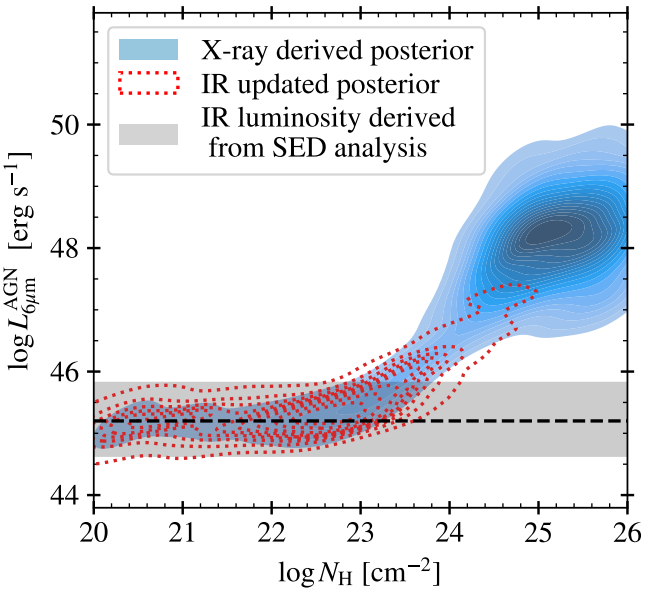


Fig. 4: Joint posterior distribution in the $\log N_H - \log L_{6\,\mu m}$ plane (blue shaded region) for source lid_1278, one of our CTK candidates. The infrared luminosity $L_{6\,\mu m}$ is inferred from the X-ray luminosity posterior via the Stern (2015) relation. The black dashed line and grey shaded region show the SED-inferred $L_{6\,\mu m}$ value and its uncertainty, while the red dotted contours indicate the posterior distribution after incorporating the IR prior.

bars) posteriors. After applying the IR constraint, only three of the original CTK candidates show probabilities above our initial selection threshold of 80%.

This result highlights the critical importance of including IR data for the reliable identification of CTK sources. Figure 1 shows that a significant number of objects in the Pouliasis et al. (2024) sample exhibit nominal N_H values above the CTK threshold but were excluded from our analysis due to low posterior probabilities of being CTK. These sources typically display broad N_H posterior distributions, and therefore the inclusion of IR constraints could substantially refine their absorption estimates.

For a complete and unbiased characterization of the CTK population—particularly in the context of high-redshift X-ray luminosity function studies (see Sect. 3.3)—it is essential to obtain IR luminosity estimates for the entire Pouliasis et al. (2024) sample. While a full SED analysis is beyond the scope of this work, we derived approximate $L_{6\,\mu m}$ values using available MIR imaging.

All fields in the sample have been observed by *Spitzer*-MIPS at 24 µm, covering the majority of the survey areas. We retrieved the flux-calibrated MIPS mosaics from the SEIP database[3] and performed aperture photometry at the optical counterpart positions of all sources in the Pouliasis et al. (2024) catalogue. This yielded observed 24 µm fluxes for the majority of sources. By adopting a representative AGN template from the `CIGALE` library, redshifting it appropriately, and scaling to the observed 24 µm flux, we estimated rest-frame $L_{6\,\mu m}$ values. Using this method, we derived IR luminosity estimates for 574 out of 811 sources in the Pouliasis et al. (2024) sample. 236 sources in the XXL-N field lie outside the MIPS coverage, so we could not estimate IR luminosities for those sources.

These $L_{6\,\mu m}$ values should be interpreted as upper limits, since we did not account for potential contamination from host galaxy emission or blending with nearby sources. To incorporate these estimates into the X-ray analysis, we updated the posterior distributions using a conservative prior on L_X. Instead of a Gaussian, we used a step function prior: the probability is set to zero for $\log L_X > \log L_X^{IR} + 2\sigma$, and constant otherwise, where L_X^{IR} is the X-ray luminosity predicted from $L_{6\,\mu m}$ using the Stern (2015) relation.

[3] https://irsa.ipac.caltech.edu/data/SPITZER/Enhanced/SEIP/

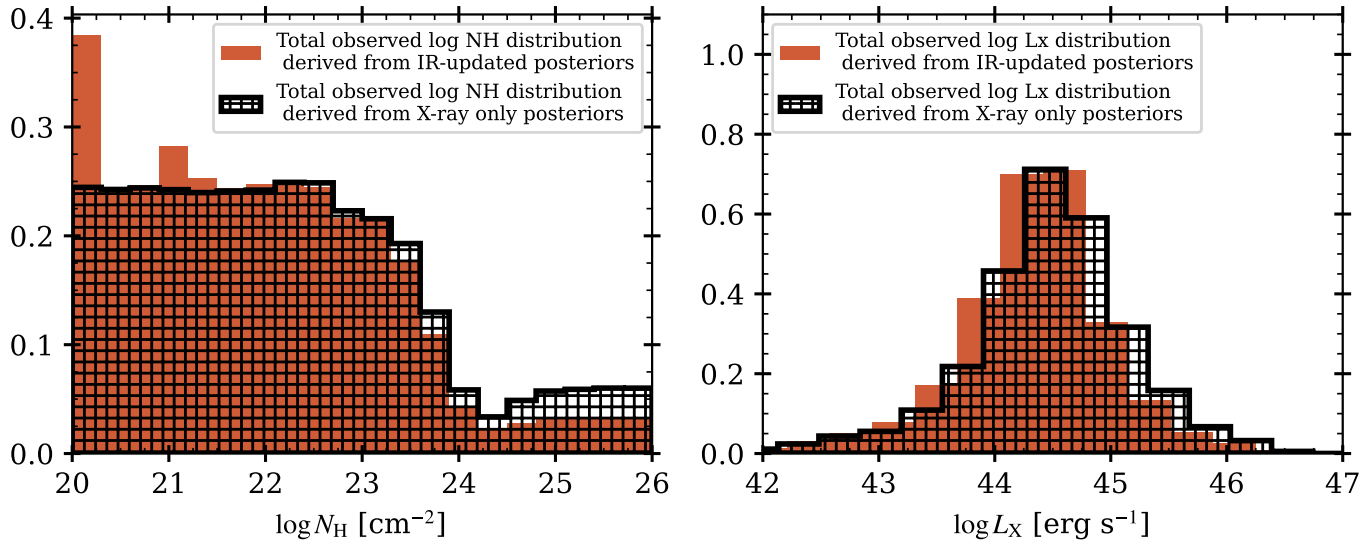


Fig. 5: Observed distributions of hydrogen column density and X-ray luminosity for the full Pouliasis et al. (2024) sample. The black-hatched histograms show the original X-ray posteriors, while the red-solid histograms correspond to the posteriors updated with IR information (see Sect. 3.2).

We validated this method by applying it to the ten CTK candidates for which we had SED-derived $L_{6\,\mu m}$ values, and found consistent results between both methods. We also tested the sensitivity of the outcome to the choice of AGN template, we recalculated the IR luminosities using an alternative AGN template and we verified that the specific template used had minimal impact on the final results, provided it corresponded to a high-inclination (edge-on) configuration.

Fig. 5 shows the impact of the IR-informed priors on the full Pouliasis et al. (2024) sample. The left and right panels display the stacked posterior distributions (Baronchelli et al. 2020, Appendix A) of N_H and log L_X, respectively. The black hatched histograms correspond to the original (X-ray-only) posteriors, while the red histograms reflect the IR-updated posteriors. While the overall L_X distribution shows a modest shift toward lower luminosities, the effect on the N_H distribution is more pronounced for the CTK population: the observed number density of CTK sources is reduced by approximately a factor of two. The distributions for unabsorbed and Compton-thin sources remain largely unaffected.

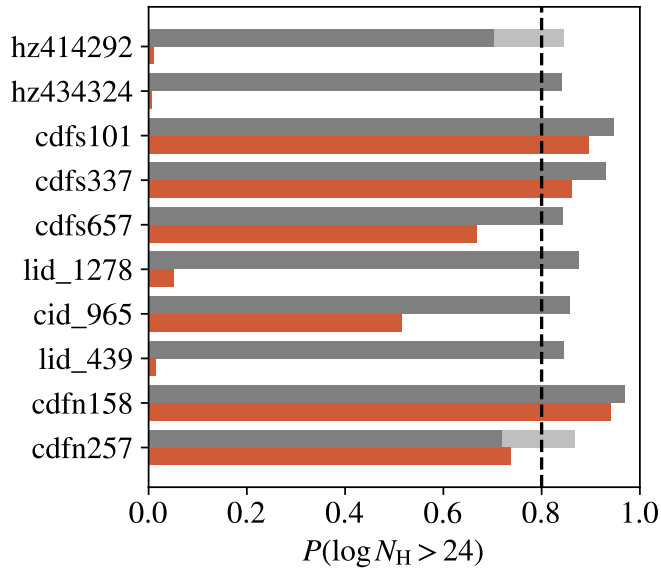


Fig. 6: Probability of the selected CTK candidates of having log $N_H > 24$. Grey bars show the original probabilities estimated using the X-ray only posteriors, and red bars show the results using the IR-updated posteriors. Light-grey areas show the estimated probabilities before applying the redshift corrections discussed in Sect. 2.1. The black dashed vertical line shows our initial selection criterion for the CTK sample.

3.3. X-ray luminosity function for CTK

The X-ray luminosity function (XLF) of AGN is a fundamental diagnostic of black hole growth and AGN evolution (Fotopoulou et al. 2016). By tracing the number density of AGN as a function of luminosity and redshift, the XLF provides a robust observational constraint of accretion activity across cosmic time (Aird et al. 2015a). An additional dimension can be introduced by including the hydrogen column density, N_H, which enables the study of the cosmic evolution of the intrinsic AGN population as a function of X-ray absorption. This leads to the definition of the X-ray luminosity and absorption function (XLAF):

$$\phi_{abs}(L_X, N_H, z) = \frac{d^3N(L_X, N_H, z)}{dV\, d\log(L_X)\, d\log(N_H)} = \phi(L_X, z) \times f_{abs}(N_H, L_X, z) \quad (2)$$

where the XLAF, $\phi_{abs}(L_X, N_H, z)$, represents the number of sources N per unit comoving volume V, per logarithmic interval in luminosity and column density, as a function of L_X, N_H and z. It is commonly assumed that the XLAF can be factorised into two components (e.g. Ueda et al. 2003, 2014; Vijarnwannaluk et al. 2022): the XLF, $\phi(L_X, z)$, and the absorption function, $f_{abs}(N_H, L_X, z)$.

In this work, we follow the methodology of Pouliasis et al. (2024) to derive a parametric form of the XLAF for CTK sources in the redshift range $z = 3-6$. The XLF is parametrised as a broken power law (Barger et al. 2005) with pure density evolution (PDE; Schmidt 1968). Pouliasis et al. (2024) tested various evolutionary models for the XLF, finding no statistically significant differences among them when applied to our dataset. We adopt the PDE model here, as it offers a good description of the data with the fewest free parameters.

For the absorption function, we use the parametrisation from Pouliasis et al. (2024): a flat-step function defined over three $N_{\rm H}$ intervals, with values that depend on both redshift and X-ray luminosity. A detailed description of the XLAF parametrisation is provided in Appendix A.

As in Pouliasis et al. (2024), we employ a Bayesian inference framework to estimate simultaneously the parametric forms of the XLF and absorption function. This approach allows a rigorous propagation of the uncertainties in the X-ray spectral parameters and photometric redshifts of individual sources, encoded in their posterior probability distributions. The posterior distribution of the XLAF parameters is sampled using MLFriends (Buchner 2016; Buchner & Bauer 2017), a nested-sampling Monte Carlo algorithm implemented in the `UltraNest` package. Full details of the methodology are given in Appendix A.

In addition to the parametric modelling described above, we derived a binned representation of the XLAF using the method of Miyaji et al. (2001). This approach estimates the space density in each luminosity, $N_{\rm H}$ and redshift bin by scaling the analytical XLAF model according to the ratio of the observed to predicted number of sources,

$$\phi_{\rm bin} = \phi_{\rm mdl} \times \frac{N_{\rm obs}}{N_{\rm mdl}}, \tag{3}$$

where $N_{\rm obs}$ is the number of detected sources and $N_{\rm mdl}$ is the number expected from $\phi_{\rm mdl}$, the best-fitting XLAF model within the same bin, obtained by integrating the model over the survey sensitivity function. This method preserves the overall shape of the parametric model while providing a data-driven visualisation of the luminosity function. The uncertainties in each bin are computed assuming Poisson statistics.

Figure 7 presents our final XLAF estimates for two redshift intervals ($z = 3-4$ and $z = 4-6$) and two column density ranges ($\log N_{\rm H} = 20-24$ and $\log N_{\rm H} = 24-26$). Black solid lines and grey shaded regions show the median and 1σ uncertainty of the XLAF derived using X-ray data alone, while red lines and the corresponding shaded regions show the results obtained after including the IR-updated posteriors. In the unabsorbed and Compton-thin regimes, the results are consistent, both exhibiting similar XLF shapes, confirming the robustness of the Pouliasis et al. (2024) results. In contrast, the CTK regime shows a systematic shift towards lower space densities when the IR information is included; an expected outcome given that, as shown in Sect. 3.2, the number of CTK sources is reduced by approximately half once the infrared constraints are applied (see also Fig. 5).

The derived XLAF can also be used to estimate the intrinsic fraction of CTK AGN within our redshift range of interest. This fraction is defined as

$$f_{\rm CTK} = \frac{N(24 \leq \log N_{\rm H} \leq 26)}{N(20 \leq \log N_{\rm H} \leq 26)}, \tag{4}$$

where N represents the number of sources within the specified comoving volume and column density range, obtained by integrating the XLAF over the relevant intervals in redshift, luminosity, and $N_{\rm H}$. From our best-fitting XLAF model, we find an intrinsic CTK fraction of $f_{\rm CTK} = 0.17^{+0.12}_{-0.11}$ in the redshift range $z = 3-6$. A comparison of this estimate with previous results will be discussed in Sect. 4 below.

4. Discussion

4.1. Reliability of $N_{\rm H}$ estimates

A reasonable concern is whether *XMM-Newton* and *Chandra* that operate in a relatively soft energy band below 10 keV, can efficiently detect CTK AGN. Indeed, extending the energy range of the X-ray spectra above 10 keV e.g. using *NuSTAR* can provide accurate column density estimates especially at low redshifts (e.g. Ricci et al. 2015). However, at the redshift range explored in this work the energy turnovers due to the mild CTK absorption are expected to lie at energies above 1.5 keV. These energies are where the effective area of *XMM-Newton* and *Chandra* is the highest. Furthermore, *NuSTAR* is not sensitive enough to detect sources in the redshift range we explore in this paper. For example, Aird et al. (2015a) compiled a sample of 94 sources using the *NuSTAR* extragalactic survey program (Harrison et al. 2013) and estimated the AGN XLF. No radio-quiet AGN have been detected above a redshift of $z = 3$. Moreover, Tokayer et al. (2025) caution that *XMM-Newton* and *Chandra* spectral fits using a limited number of counts are reliable especially in the case of CTK AGN. As already mentioned above, Laloux et al. (2023) attempt to limit the effect of this constraint by employing mid-IR priors.

In Sect. 3 we examined the reliability of the X-ray–derived absorption estimates for our sample of CTK AGN candidates. By combining the X-ray spectral results with multiwavelength information, in particular the infrared constraints derived from SED fitting, we evaluated how robustly the X-ray data alone can identify genuine CTK sources across surveys of varying depth. As discussed in Sect. 3.2, the number of CTK candidates in our sample decreases from ten to three once their multiwavelength properties are examined in detail. In most cases, the derived column densities remain indicative of a heavily obscured environment, although they fall below the formal CTK threshold. This suggests that while strong absorption is present, the extreme levels implied by the initial X-ray analysis are not always robust.

The impact of introducing IR information varies across surveys. This effect is illustrated in Fig. 6 where we show the probabilities of our selected CTK candidates of having $\log N_{\rm H} > 24$ derived from the corresponding posteriors before and after updating with the IR information. Sources in the *Chandra* Deep Fields are the least affected, owing to the significantly longer exposure times in these regions. Their spectra typically contain more than 100 net counts, allowing for a reliable detection of the Fe K_α emission line expected in CTK AGN (George & Fabian 1991) and providing well-constrained estimates of $N_{\rm H}$ based solely on the X-ray data.

In contrast, the CTK candidates identified in the shallower CCLS and XXL-N surveys have much lower-count spectra, often containing only a few tens of counts. While the overall continuum shape in these cases is consistent with high absorption, the inferred $N_{\rm H}$ values are considerably less secure. In such low signal-to-noise regimes, apparent CTK classifications may be driven by Poisson fluctuations near the observed energy of the Fe K_α line rather than by genuine spectral features.

These results highlight that only high signal-to-noise X-ray observations can reliably constrain $N_{\rm H}$ in the CTK regime at

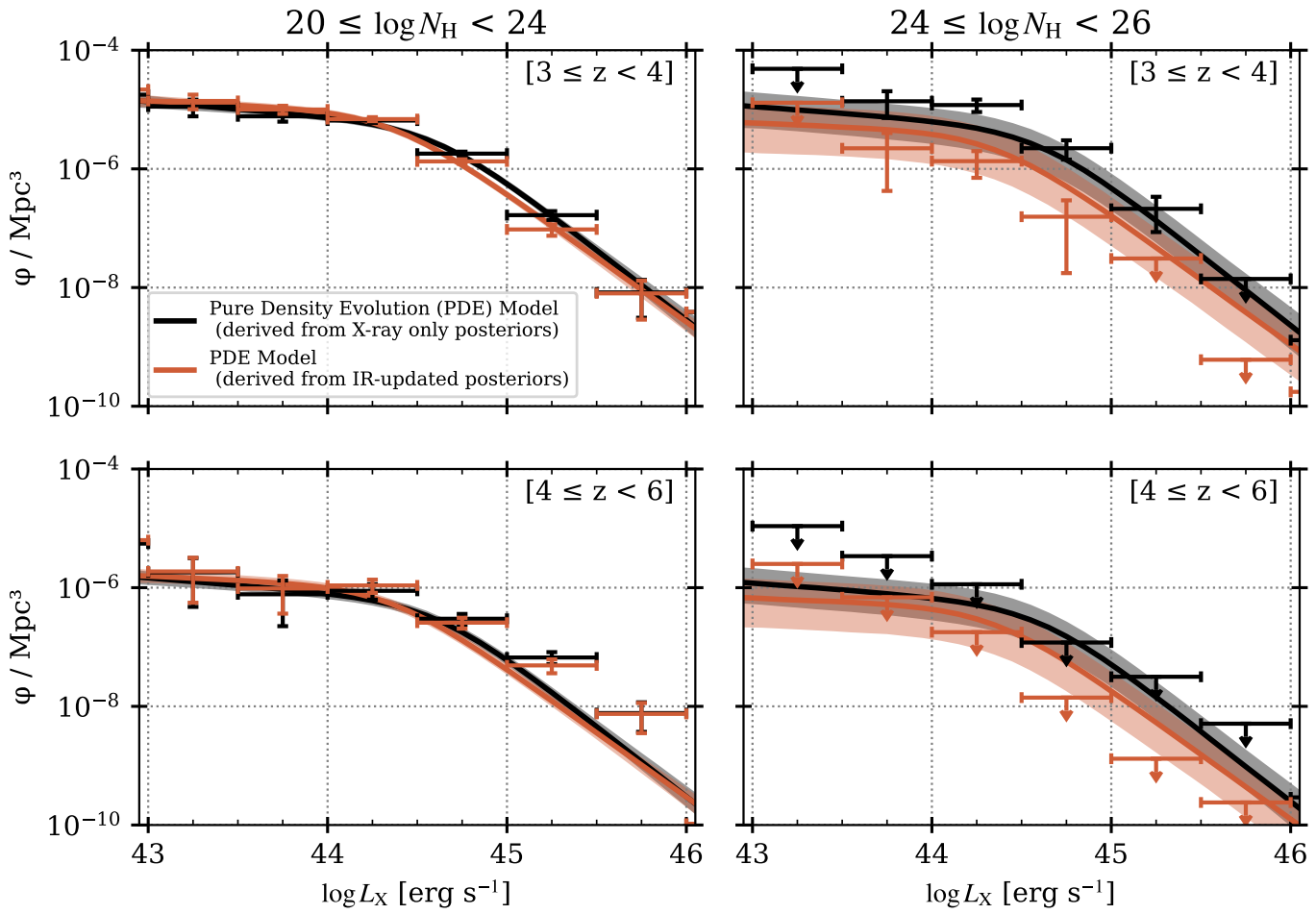


Fig. 7: X-ray luminosity and absorption function for two redshift intervals ($z = 3-4$, top panels; $z = 4-6$, bottom panels) and two hydrogen column density ranges ($\log N_H = 20-24$, left panels; $\log N_H = 24-26$, right panels). Black lines and grey shaded regions indicate the results for the parametric XLAF obtained from the X-ray-only posteriors, while red lines and shaded regions correspond to those derived using the IR luminosity priors. The corresponding binned XLAFs were derived using the Miyaji et al. (2001) method.

these redshifts. For the majority of current *XMM-Newton* and *Chandra* surveys, the available depth is insufficient for a robust identification of CTK sources at high redshift based on X-ray data alone. Incorporating complementary IR information is therefore essential to obtain a reliable census of the most heavily obscured AGN.

4.2. The CTK AGN luminosity function

Section 3.3 presented our estimates of the XLF for the high-redshift CTK AGN population. In that analysis, we tested the impact of incorporating IR–updated priors into the X-ray spectral fitting results. The inclusion of IR information systematically shifts the inferred space densities towards lower values, reflecting a more conservative and physically consistent view of the CTK population. The discussion that follows refers exclusively to these IR-updated results.

The binned luminosity function (Fig. 7) shows that our data provide meaningful constraints on the CTK population only within the $z = 3-4$ redshift interval and over the luminosity range $43.5 \leq \log L_X \leq 45$. At lower luminosities, the CTK population remains essentially unconstrained, as the current surveys lack the sensitivity required to reliably detect CTK sources below $\log L_X \sim 43$ at these redshifts. Similarly, for $z = 4-6$, the XLF is constrained only by upper limits, indicating that the available data are insufficient to fully characterise the evolution of the most heavily obscured AGN at these epochs.

It should also be noted that the Pouliasis et al. (2024) sample is selected in the soft X-ray band (0.5–2 keV). At the redshifts considered here, this energy range approximately corresponds to the rest-frame hard band (2–10 keV), which may lead to the exclusion of the most extremely obscured, reflection-dominated CTK sources. Indeed, our sample does not include some known high-z CTK AGN, such as the $z = 4.762$ source in the CDF-S reported by Gilli et al. (2014). These selection effects should be kept in mind when interpreting our results, as they imply that our parametric estimates of the X-ray luminosity and absorption function rely partly on extrapolations in luminosity and redshift regimes where direct observational constraints are limited.

Figure 8 presents our final CTK XLF for $z = 3-6$, compared with previous studies. We include the high-redshift CTK XLFs of Buchner et al. (2015) and Aird et al. (2015b), as well as the local ($z < 0.05$) CTK XLF derived by Georgantopoulos et al. (2025). The latter was obtained from a *Swift*-BAT-selected sample of local AGN, with N_H values measured using *NuSTAR* observations. The high-z studies by Buchner et al. (2015) and

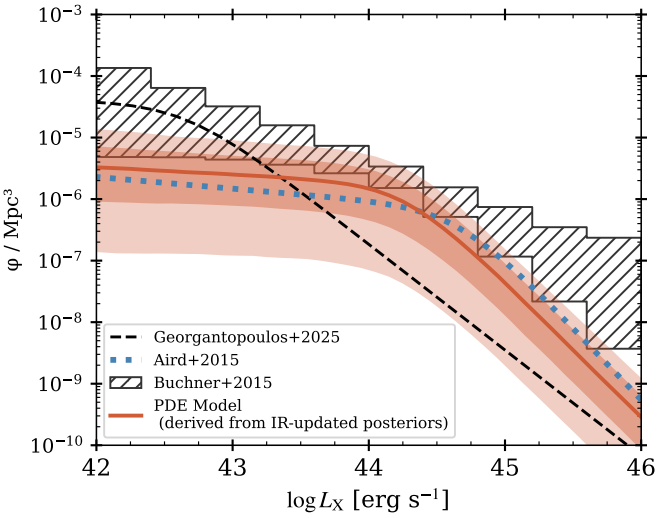


Fig. 8: X-ray luminosity function for the CTK population ($24 < \log N_{\rm H} < 26$). Red symbols show our result for the parametric XLF in the 3–6 redshift range. The red solid line corresponds to the median value and shaded areas are the 1σ (darker red) and 2σ (lighter red) uncertainties. The black-dashed line is the XLF for CTK sources in the local universe ($z < 0.05$) derived by Georgantopoulos et al. (2025). The grey, hatched area is the non-parametric XLF in the 3.1–7 redshift range estimated by Buchner et al. (2015). The area shows the 90% confidence region. The blue-dotted line corresponds to the Aird et al. (2015b) XLF for CTK AGN in the 3–6 redshift range.

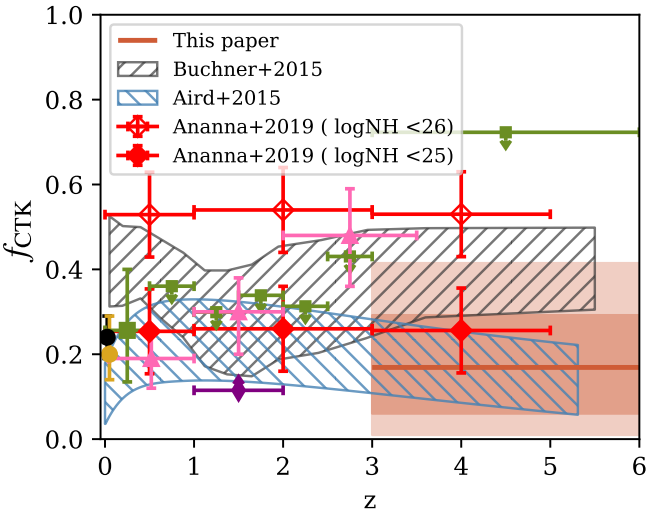


Fig. 9: Evolution of the fraction of CTK sources over the total AGN population across redshift. Our results are shown with the red shaded regions that represent the 1σ (darker red) and 2σ (lighter red) confidence regions. The gray-hatched area corresponds to the Buchner et al. (2015) results (90% confidence interval) for AGN in the $43.2 \leq \log L_{\rm X} \leq 43.6$ interval. The blue-hatched area shows the Aird et al. (2015b) estimates (99% confidence interval) for sources with $\log L_{\rm X} = 43.5$. The green squares show the results by Laloux et al. (2023); quoted upper-limits are 3σ. Pink triangles correspond to the results by Lanzuisi et al. (2018) and purple diamond corresponds to a study by Masini et al. (2018). The black (Georgantopoulos et al. 2025) and yellow (Burlon et al. 2011) circles show the CTK fraction in the local universe using *Swift*-BAT selected AGN. Red diamonds show the fraction of CTK sources estimated through the integration of the Ananna et al. (2019) luminosity function. Open symbols show the result in the range ($24 \leq \log N_{\rm H} < 26$), while filled symbols are for ($24 \leq \log N_{\rm H} < 25$).

Aird et al. (2015b) were selected because they are based on X-ray surveys similar to ours—combining deep, pencil-beam observations with shallower, wide-area fields (using *Chandra* and *XMM-Newton* observations)—and employ comparable Bayesian methodologies to infer the luminosity function. The principal distinction lies in their functional forms: Buchner et al. (2015) adopted a non-parametric approach, whereas Aird et al. (2015b) employed a parametric model. The latter, a flexible double power-law formulation, allows all parameters of the double power law to evolve as polynomial functions of $\log(1+z)$, thereby accommodating redshift-dependent variations in the XLF shape driven by the data. We also compared with the XLAF of (Ananna et al. 2019). This luminosity function is derived from a population synthesis model aiming to reproduce the Cosmic X-ray Background and the observed counts of CTK-AGN in surveys with *XMM-Newton*, *Chandra*, NuSTAR and *Swift*-BAT.

Our results are consistent with Aird et al. (2015b) and systematically lower than those reported by Buchner et al. (2015). When compared to the local Universe, our XLF indicates a substantially lower space density of CTK sources at low luminosities ($\log L_{\rm X} < 43$), while all studies show an increasing density towards higher luminosities ($\log L_{\rm X} > 44$). Interestingly, the local XLF of Georgantopoulos et al. (2025) aligns closely with the low-luminosity end of the Buchner et al. (2015) results.

The discrepancy between our results and those of Buchner et al. (2015) may stem from methodological differences. Their analysis relied solely on X-ray data, without the benefit of IR constraints, which, as we have shown, tend to reduce the inferred CTK number densities. However, the consistency between our IR-informed results and those of Aird et al. (2015b), which were also based exclusively on X-ray data, suggests that additional factors may be at play. A key distinction is that Buchner et al. (2015) derived individual source properties through full spectral modelling, similar to our approach, whereas Aird et al. (2015b) employed broad-band count-rate analyses. It is likely that the latter method is less prone to spurious identification of CTK sources, as it does not rely on detailed spectral features, such as the Fe K_α line, that can be affected by low-count statistical fluctuations.

Overall, our results suggest that the space density of CTK AGN at $z = 3-6$ is lower than previously inferred from X-ray data alone, although the uncertainties remain substantial due to limited statistics and selection biases. The consistency between our IR-informed analysis and independent parametric estimates reinforces the robustness of our approach, while also highlighting the need for deeper, high-energy observations–such as those anticipated from *NewAthena* and other future missions–to fully characterise the obscured growth of supermassive black holes in the early Universe.

4.3. The evolution of the CTK fraction

Figure 9 compares our estimates of the CTK fraction[4] in the redshift range $z = 3-6$ with previous measurements span-

[4] Our results for the CTK fraction are derived from our estimate of the XLAF (see Eq. 4), which takes into account the likelihood of

ning from the local Universe up to $z \sim 6$. The results from Buchner et al. (2015) and Aird et al. (2015b) are derived from the luminosity functions presented in Sect. 4.2. The estimates of Lanzuisi et al. (2018) are based on a study of CTK AGN selected in the CCLS, while those of Laloux et al. (2023) also rely on CCLS data but employ a non-parametric approach to model the X-ray luminosity and absorption function of the AGN population. In the latter work, X-ray spectral fitting was performed for individual sources using IR–derived priors. The measurement by Masini et al. (2018) originates from a *NuSTAR* survey of the UKIDSS Ultra Deep Survey field and represents the observed CTK fraction, which can be considered a lower limit to the intrinsic value. For comparison, we also include two estimates of the CTK fraction for the local Universe from Burlon et al. (2011) and Georgantopoulos et al. (2025). Additionally, we have incorporated the CTK fractions estimated through the integration of the luminosity function estimated by Ananna et al. (2019). We calculated the CTK fraction across two different $N_{\rm H}$ intervals ($24 \leq \log N_{\rm H} \leq 25$, and $24 \leq \log N_{\rm H} \leq 26$).

Among these studies, the results of Buchner et al. (2015) and Lanzuisi et al. (2018) stand out for their remarkably high CTK fraction of approximately 40-50%, among the largest values reported in the literature at high redshift. Such high fractions are, however, in clear tension with both our findings and those of other works. For example, Aird et al. (2015b) reported lower CTK fractions that are broadly consistent with our results in the $z = 3 - 6$ range, although they noted that their highest-redshift bins may be affected by limited statistics. The results of Ananna et al. (2019) show no evolution with redshift and, for the population with $\log N_{\rm H} < 25$, the CTK fraction is about 30 per cent, consistent with previous results in similar redshift ranges. The estimate for the high redshift range ($3 < z < 5$) aligns with our estimate of the CTK fraction at high redshifts. However, when considering the population with $\log N_{\rm H} > 25$, the CTK fraction from Ananna et al. (2019) reaches $\sim 50\%$ that is similar to the highest values reported in the literature(Lanzuisi et al. 2018). This discrepancy may arise from the limited sensitivity to this highly absorbed population in the X-ray energies examined by these studies.

At intermediate redshifts ($0.5 < z < 2.5$), most studies converge on a CTK fraction of 15–30%, consistent with estimates for the local Universe. Overall, the emerging picture suggests no compelling evidence for strong evolution of the CTK fraction up to $z \approx 5 - 6$. The only study reporting a significant increase is that of Lanzuisi et al. (2018), who found a rise from $\sim 20\%$ at low redshift to nearly 50% at $z \sim 3$. These results appear to be in tension with the more recent analysis by Laloux et al. (2023) of the same field, whose upper limits around $z \sim 3$ favour a lower CTK fraction than that inferred by Lanzuisi et al. (2018).

In contrast, the evolution of the total obscured AGN population (including Compton-thin sources) is well established (e.g. Vito et al. 2018; Signorini et al. 2023; Peca et al. 2023; Pouliasis et al. 2024), showing a pronounced increase towards higher redshifts. This trend may be explained by the findings of Gilli et al. (2022), who proposed that the rise in the obscured AGN population is primarily linked to the interstellar medium (ISM) of the host galaxies. Their model suggests that ISM-driven obscuration rarely reaches the CTK regime at these redshifts. Instead, the ISM is expected to dominate obscuration within the Compton-thin range, while the relative contribution of CTK sources remains approximately constant across cosmic time.

These findings support a scenario in which the most heavily obscured, CTK phase of AGN activity represents a relatively stable component of black hole growth. The strong redshift evolution observed in the overall obscured population is therefore likely driven by increasing Compton-thin obscuration associated with the evolving ISM of high-redshift galaxies (Scoville et al. 2014, 2017).

5. Conclusions

We investigated the population of CTK AGN at high redshift ($z \geq 3$) using the Pouliasis et al. (2024) sample, one of the largest X-ray–selected AGN datasets currently available in this regime. From this sample, we identified a subsample of ten high-probability CTK candidates based on the Bayesian X-ray spectral fits of Pouliasis et al. (2024) and examined their multiwavelength properties through SED analysis to assess the robustness of their CTK classifications. While the SEDs are generally consistent with heavily obscured AGN, a substantial fraction of the sources exhibit X-ray luminosities significantly higher than expected from the established correlations between $L_{\rm X}$ and $L_{6\,\mu{\rm m}}$. Most of these outliers have low-count X-ray spectra, suggesting that the discrepancy arises from an overestimate of $N_{\rm H}$.

To address this, we applied the methodology of Laloux et al. (2023) to update the X-ray posterior distributions with the IR constraints derived from our SED analysis, yielding more physically consistent X-ray properties. After this update, only three sources retained a high probability of being CTK, while the others still showed substantial absorption but below the nominal CTK threshold.

We then derived the X-ray luminosity function (XLF) for CTK AGN in parametric form, using the complete sample and methodology of Pouliasis et al. (2024). The individual X-ray posteriors were updated using $L_{6\,\mu{\rm m}}$ upper limits estimated from *Spitzer*-MIPS 24 μm photometry to obtain more robust values for $L_{\rm X}$ and $N_{\rm H}$. Incorporating IR constraints systematically reduces the inferred space density of CTK AGN, resulting in a more conservative and physically consistent description of the population, while leaving the unabsorbed and Compton-thin XLF largely unaffected. The resulting CTK XLF provides meaningful constraints for $z = 3 - 4$ and $43.5 \lesssim \log L_{\rm X} \lesssim 45$, whereas at lower luminosities and higher redshifts the data remain limited by current survey sensitivities.

Our derived CTK XLF is consistent with that of Aird et al. (2015b) and lower than the estimates of Buchner et al. (2015), underscoring the importance of multiwavelength constraints in mitigating degeneracies in X-ray spectral fitting. We find an intrinsic CTK fraction of $f_{\rm CTK} = 0.17^{+0.12}_{-0.11}$ in the redshift range $z = 3-6$. Comparisons with local and intermediate-redshift measurements indicate that the CTK space density remains broadly stable with redshift, in contrast to the overall obscured AGN population (including Compton-thin sources), which shows strong evolution towards higher redshift. This trend likely reflects increasing interstellar medium obscuration in high-redshift galaxies, while the intrinsic CTK fraction remains approximately constant across cosmic time.

Overall, our results support a scenario in which the CTK phase represents a persistent but relatively rare mode of black hole growth, contributing a stable fraction to the accretion history of the Universe. Future high-sensitivity, broad-band X-ray observatories such as *NewAthena* and *HEX-P* will be essential to further constrain this population, extending current analyses to lower luminosities and providing a more robust census of the most heavily obscured AGN at early cosmic epochs.

sources being detected/undetected as functions of, $L_{\rm X}, z$, and $N_{\rm H}$ (see Appendix A.

Acknowledgements. The research leading to these results has received funding from the Hellenic Foundation for Research and Innovation (HFRI) project "4MOVE-U" grant agreement 2688, which is part of the programme "2nd Call for HFRI Research Projects to support Faculty Members and Researchers". EP and IG acknowledge ACME, a project funded by the European Union's Horizon Europe Research and Innovation programme under Grant Agreement 101131928. Based on observations obtained with *XMM-Newton*, an ESA science mission with instruments and contributions directly funded by ESA member states and NASA. This research has made use of data obtained from the *Chandra* Data Archive and the *Chandra* Source Catalogue, and software provided by the *Chandra* X-ray Center (CXC) in the application packages CIAO and Sherpa. This research has made use of the NASA/IPAC Infrared Science Archive, which is funded by the National Aeronautics and Space Administration and operated by the California Institute of Technology. This work is based on observations made with the *Spitzer* Space Telescope, which is operated by the Jet Propulsion Laboratory, California Institute of Technology under a contract with NASA. This work made use of Astropy:[5] a community-developed core Python package and an ecosystem of tools and resources for astronomy (Astropy Collaboration et al. 2013, 2018, 2022). The plots in this publication were produced using Matplotlib, a Python library for publication-quality graphics (Hunter 2007).

References

Aird, J., Alexander, D. M., Ballantyne, D. R., et al. 2015a, ApJ, 815, 66
Aird, J., Coil, A. L., Georgakakis, A., et al. 2015b, MNRAS, 451, 1892
Akylas, A., Georgakakis, A., Georgantopoulos, I., Brightman, M., & Nandra, K. 2012, A&A, 546, A98
Akylas, A., Georgantopoulos, I., Gandhi, P., Boorman, P., & Greenwell, C. L. 2024, A&A, 692, A250
Akylas, A., Georgantopoulos, I., Ranalli, P., et al. 2016, A&A, 594, A73
Alexander, D. M., Chary, R. R., Pope, A., et al. 2008, ApJ, 687, 835
Alexander, D. M. & Hickox, R. C. 2012, New A Rev., 56, 93
Ananna, T. T., Treister, E., Urry, C. M., et al. 2019, ApJ, 871, 240
Annuar, A., Alexander, D. M., Gandhi, P., et al. 2025, MNRAS, 540, 3827
Antonucci, R. R. J. & Miller, J. S. 1985, ApJ, 297, 621
Ashby, M. L. N., Stanford, S. A., Brodwin, M., et al. 2013, ApJS, 209, 22
Astropy Collaboration, Price-Whelan, A. M., Lim, P. L., et al. 2022, ApJ, 935, 167
Astropy Collaboration, Price-Whelan, A. M., Sipőcz, B. M., et al. 2018, AJ, 156, 123
Astropy Collaboration, Robitaille, T. P., Tollerud, E. J., et al. 2013, A&A, 558, A33
Barger, A. J., Cowie, L. L., Mushotzky, R. F., et al. 2005, AJ, 129, 578
Baronchelli, L., Nandra, K., & Buchner, J. 2020, MNRAS, 498, 5284
Barthelmy, S. D., Barbier, L. M., Cummings, J. R., et al. 2005, Space Sci. Rev., 120, 143
Boorman, P. G., Gandhi, P., Buchner, J., et al. 2025, ApJ, 978, 118
Boquien, M., Burgarella, D., Roehlly, Y., et al. 2019, A&A, 622, A103
Brandt, W. N. & Alexander, D. M. 2015, A&A Rev., 23, 1
Brightman, M., Nandra, K., Salvato, M., et al. 2014, MNRAS, 443, 1999
Bruzual, G. & Charlot, S. 2003, MNRAS, 344, 1000
Buchner, J. 2016, Statistics and Computing, 26, 383
Buchner, J. 2021, The Journal of Open Source Software, 6, 3001
Buchner, J. & Bauer, F. E. 2017, MNRAS, 465, 4348
Buchner, J., Brightman, M., Nandra, K., Nikutta, R., & Bauer, F. E. 2019, A&A, 629, A16
Buchner, J., Georgakakis, A., Nandra, K., et al. 2015, ApJ, 802, 89
Buchner, J., Georgakakis, A., Nandra, K., et al. 2014, A&A, 564, A125
Burlon, D., Ajello, M., Greiner, J., et al. 2011, ApJ, 728, 58
Carroll, C. M., Hickox, R. C., Masini, A., et al. 2021, ApJ, 908, 185
Charlot, S. & Fall, S. M. 2000, ApJ, 539, 718
Chen, C.-T. J., Hickox, R. C., Goulding, A. D., et al. 2017, ApJ, 837, 145
Civano, F., Marchesi, S., Comastri, A., et al. 2016, ApJ, 819, 62
Comastri, A., Setti, G., Zamorani, G., & Hasinger, G. 1995, A&A, 296, 1
Dale, D. A., Helou, G., Magdis, G. E., et al. 2014, ApJ, 784, 83
Edge, A., Sutherland, W., Kuijken, K., et al. 2013, The Messenger, 154, 32
Fotopoulou, S., Buchner, J., Georgantopoulos, I., et al. 2016, A&A, 587, A142
García-Burillo, S., Combes, F., Ramos Almeida, C., et al. 2016, ApJ, 823, L12
Georgakakis, A., Aird, J., Buchner, J., et al. 2015, MNRAS, 453, 1946
Georgakakis, A., Salvato, M., Liu, Z., et al. 2017, MNRAS, 469, 3232
Georgantopoulos, I. & Akylas, A. 2019, A&A, 621, A28
Georgantopoulos, I., Comastri, A., Vignali, C., et al. 2013, A&A, 555, A43
Georgantopoulos, I., Pouliasis, E., Ruiz, A., & Akylas, A. 2025, A&A, 695, A128
Georgantopoulos, I., Rovilos, E., Akylas, A., et al. 2011, A&A, 534, A23
George, I. M. & Fabian, A. C. 1991, MNRAS, 249, 352
Giavalisco, M., Ferguson, H. C., Koekemoer, A. M., et al. 2004, ApJ, 600, L93
Gilli, R., Comastri, A., & Hasinger, G. 2007, A&A, 463, 79
Gilli, R., Norman, C., Calura, F., et al. 2022, A&A, 666, A17
Gilli, R., Norman, C., Vignali, C., et al. 2014, A&A, 562, A67
Grogin, N. A., Kocevski, D. D., Faber, S. M., et al. 2011, ApJS, 197, 35
Haardt, F. & Maraschi, L. 1991, ApJ, 380, L51
Harrison, F. A., Craig, W. W., Christensen, F. E., et al. 2013, ApJ, 770, 103
Hasinger, G., Miyaji, T., & Schmidt, M. 2005, A&A, 441, 417
Hönig, S. F., Kishimoto, M., Antonucci, R., et al. 2012, ApJ, 755, 149
Hunter, J. D. 2007, Computing in Science and Engineering, 9, 90
IRSA & SSC. 2020, Spitzer Enhanced Imaging Products, NASA IPAC DataSet, IRSA433
Jarvis, M. J., Bonfield, D. G., Bruce, V. A., et al. 2013, MNRAS, 428, 1281
Kloek, T. & van Dijk, H. K. 1978, Econometrica, 46, 1
Koekemoer, A. M., Faber, S. M., Ferguson, H. C., et al. 2011, ApJS, 197, 36
Komatsu, E., Dunkley, J., Nolta, M. R., et al. 2009, ApJS, 180, 330
Laloux, B., Georgakakis, A., Andonie, C., et al. 2023, MNRAS, 518, 2546
Lanzuisi, G., Civano, F., Marchesi, S., et al. 2018, MNRAS, 480, 2578
Lanzuisi, G., Ranalli, P., Georgantopoulos, I., et al. 2015, A&A, 573, A137
Lawrence, A., Warren, S. J., Almaini, O., et al. 2007, MNRAS, 379, 1599
Loredo, T. J. 2004, in American Institute of Physics Conference Series, Vol. 735, Bayesian Inference and Maximum Entropy Methods in Science and Engineering, ed. R. Fischer, R. Preuss, & U. V. Toussaint, 195–206
Luo, B., Brandt, W. N., Xue, Y. Q., et al. 2017, ApJS, 228, 2
Lynden-Bell, D. 1969, Nature, 223, 690
Marchesi, S., Civano, F., Elvis, M., et al. 2016, ApJ, 817, 34
Masini, A., Civano, F., Comastri, A., et al. 2018, ApJS, 235, 17
Mateos, S., Carrera, F. J., Alonso-Herrero, A., et al. 2015, MNRAS, 449, 1422
McMahon, R. G., Banerji, M., Gonzalez, E., et al. 2013, The Messenger, 154, 35
Miyaji, T., Hasinger, G., Salvato, M., et al. 2015, ApJ, 804, 104
Miyaji, T., Hasinger, G., & Schmidt, M. 2000, A&A, 353, 25
Miyaji, T., Hasinger, G., & Schmidt, M. 2001, A&A, 369, 49
Miyazaki, S., Komiyama, Y., Kawanomoto, S., et al. 2018, PASJ, 70, S1
Nenkova, M., Sirocky, M. M., Ivezić, Ž., & Elitzur, M. 2008a, ApJ, 685, 147
Nenkova, M., Sirocky, M. M., Nikutta, R., Ivezić, Ž., & Elitzur, M. 2008b, ApJ, 685, 160
Netzer, H. 2015, ARA&A, 53, 365
Peca, A., Cappelluti, N., Urry, C. M., et al. 2023, ApJ, 943, 162
Pierre, M., Pacaud, F., Adami, C., et al. 2016, A&A, 592, A1, (XXL Paper I)
Pouliasis, E., Mountrichas, G., Georgantopoulos, I., et al. 2022, A&A, 667, A56
Pouliasis, E., Ruiz, A., Georgantopoulos, I., et al. 2024, A&A, 685, A97
Press, W. H., Teukolsky, S. A., Vetterling, W. T., & Flannery, B. F. 2007, Numerical Recipes: The Art of Scientific Computing (Cambridge University Press)
Ricci, C., Ueda, Y., Koss, M. J., et al. 2015, ApJ, 815, L13
Sajina, A., Lacy, M., & Pope, A. 2022, Universe, 8, 356
Salpeter, E. E. 1955, ApJ, 121, 161
Sawicki, M., Arnouts, S., Huang, J., et al. 2019, MNRAS, 489, 5202
Schartmann, M., Meisenheimer, K., Camenzind, M., Wolf, S., & Henning, T. 2005, A&A, 437, 861
Schmidt, M. 1968, ApJ, 151, 393
Scoville, N., Aussel, H., Sheth, K., et al. 2014, ApJ, 783, 84
Scoville, N., Lee, N., Vanden Bout, P., et al. 2017, ApJ, 837, 150
Severgnini, P., Caccianiga, A., & Della Ceca, R. 2012, A&A, 542, A46
Shirley, R., Duncan, K., Campos Varillas, M. C., et al. 2021, MNRAS, 507, 129
Signorini, M., Marchesi, S., Gilli, R., et al. 2023, A&A, 676, A49
Stalevski, M., Fritz, J., Baes, M., Nakos, T., & Popović, L. Č. 2012, MNRAS, 420, 2756
Stalevski, M., Ricci, C., Ueda, Y., et al. 2016, MNRAS, 458, 2288
Stern, D. 2015, ApJ, 807, 129
Straatman, C. M. S., Spitler, L. R., Quadri, R. F., et al. 2016, ApJ, 830, 51
Toba, Y., Ueda, Y., Matsuoka, K., et al. 2019, MNRAS, 484, 196
Tokayer, Y. M., Koss, M. J., Urry, C. M., et al. 2025, ApJ, 982, 134
Torres-Albà, N., Marchesi, S., Zhao, X., et al. 2021, ApJ, 922, 252
Ueda, Y., Akiyama, M., Hasinger, G., Miyaji, T., & Watson, M. G. 2014, ApJ, 786, 104
Ueda, Y., Akiyama, M., Ohta, K., & Miyaji, T. 2003, ApJ, 598, 886
Vijarnwannaluk, B., Akiyama, M., Schramm, M., et al. 2024, MNRAS, 529, 3610
Vijarnwannaluk, B., Akiyama, M., Schramm, M., et al. 2022, ApJ, 941, 97
Vito, F., Brandt, W. N., Yang, G., et al. 2018, MNRAS, 473, 2378
Weaver, J. R., Kauffmann, O. B., Ilbert, O., et al. 2022, ApJS, 258, 11
Xue, Y. Q., Luo, B., Brandt, W. N., et al. 2016, ApJS, 224, 15

[5] http://www.astropy.org

Appendix A: Calculation of the X-ray luminosity and absorption function

This appendix describes the parametric modelling of the X-ray luminosity and absorption functions used to characterise the high-redshift AGN population analysed in this work. We outline the adopted analytical forms for the luminosity and absorption distributions, their assumed redshift evolution, and the Bayesian framework employed to constrain the model parameters.

Parametric form for the XLAF

We modelled the differential X-ray luminosity function assuming a broken power-law form, which has been shown to describe well the shape of the local AGN population. It is defined as:

$$\phi(L_{\rm X}, z=0) = \frac{{\rm d}\Phi(L_{\rm X}, z=0)}{{\rm d}\log L_{\rm X}} = A \times \left[\left(\frac{L_{\rm X}}{L_*}\right)^{\gamma_1} + \left(\frac{L_{\rm X}}{L_*}\right)^{\gamma_2}\right]^{-1}, \tag{A.1}$$

where A is the normalisation factor, L_* is the characteristic luminosity break, and γ_1 and γ_2 are the slopes of the power law before and after L_*, respectively (Miyaji et al. 2000; Hasinger et al. 2005).

To account for cosmic evolution, we adopted a pure density evolution model (PDE; Schmidt 1968), in which the luminosity function varies with redshift according to:

$$\phi(L_{\rm X}, z) = \frac{{\rm d}\Phi(L_{\rm X}, z=0)}{{\rm d}\log L_{\rm X}} \times e(z), \tag{A.2}$$

where $e(z)$ characterises the redshift evolution of the local luminosity function and is expressed as

$$e(z) = \left(\frac{1+z}{1+z_c}\right)^{p_{\rm den}}. \tag{A.3}$$

Given our definition for the XLAF (see Eq. 2, Sect. 3.3), we need to assume a functional form for the absorption function, $f_{\rm abs}$.Following the methodology of Ueda et al. (2003), we modelled the absorption function using piecewise constant functions across discrete $N_{\rm H}$ bins. Given the redshift range of our study and the energy coverage of *XMM-Newton* and *Chandra*, X-ray absorption cannot be reliably constraint for column densities below $\sim 10^{23}$ cm^{-2}. We therefore defined the absorption function in three $N_{\rm H}$ intervals as follows:

$$f_{\rm abs}(N_{\rm H}, z, L_{\rm X}) = \begin{cases} \dfrac{1}{3} - \dfrac{\varepsilon}{3(1+\varepsilon)}\psi(z, L_{\rm X}) & [20 \leq \log N_{\rm H} < 23] \\ \dfrac{\varepsilon}{1+\varepsilon}\psi(z, L_{\rm X}) & [23 \leq \log N_{\rm H} < 24] \\ \dfrac{f_{{\rm CTK},r}}{2}\,\psi(z, L_{\rm X}) & [24 \leq \log N_{\rm H} < 26] \end{cases} \tag{A.4}$$

In this parametrisation, ε represents the ratio between the number of sources with $23 \leq \log N_{\rm H} < 24$ and those with $22 \leq \log N_{\rm H} < 23$, while $f_{{\rm CTK},r}$ denotes the relative fraction of CTK sources with respect to absorbed Compton-thin AGN (Vijarnwannaluk et al. 2022).

The quantity $\psi(z, L_{\rm X})$ corresponds to the fraction of absorbed Compton-thin AGN relative to the total AGN population. It incorporates both the redshift and luminosity dependence and is parametrised as a linear function of $\log L_{\rm X}$:

$$\psi(z, L_{\rm X}) = \min(\psi_{\rm max}, \max(\psi_{43.75}(z) - C(\log L_{\rm X} - 43.75), \psi_{\rm min})), \tag{A.5}$$

where we adopt $\psi_{\rm min} = 0.2$ and $\psi_{\rm max} = 0.99$. The parameter C controls the luminosity dependence, while $\psi_{43.75}(z)$ represents the absorption fraction for AGN with $\log L_{\rm X} = 43.75$ at a given redshift.

For $z < 2$, $\psi_{43.75}(z)$ is well constrained (Ueda et al. 2014), whereas above this redshift it is typically assumed constant (e.g. $2 \leq z < 3$; Vijarnwannaluk et al. 2022). In this work, we extended the definition of $\psi_{43.75}(z)$ for $z \geq 3$ as:

$$\psi_{43.75}(z \geq 3) = \psi_3 \times (1+z)^{a_2}, \tag{A.6}$$

where ψ_3 denotes the absorption fraction at $\log L_{\rm X} = 43.75$ and $z = 3$, and a_2 is the redshift evolution index.

Bayesian inference framework

We employed a Bayesian approach to estimate simultaneously the parametric form of the XLF and the absorption function. Given a dataset of n observations, $D = \{d_i; i = 1, \ldots, n\}$, and a model for the XLF described by a set of parameters $\mathbf{\Theta}$, Bayes' theorem gives:

$$P(\mathbf{\Theta}|D) = \frac{P(D|\mathbf{\Theta})P(\mathbf{\Theta})}{P(D)}, \tag{A.7}$$

where $P(\mathbf{\Theta}|D)$ is the posterior probability of the model given the data, $\mathscr{L} = P(D|\mathbf{\Theta})$ is the likelihood of obtaining the data for a given model, $P(\mathbf{\Theta})$ is the prior probability of the model parameters, and $P(D) = \int P(\mathbf{\Theta}|D){\rm d}\mathbf{\Theta}$ is the evidence.

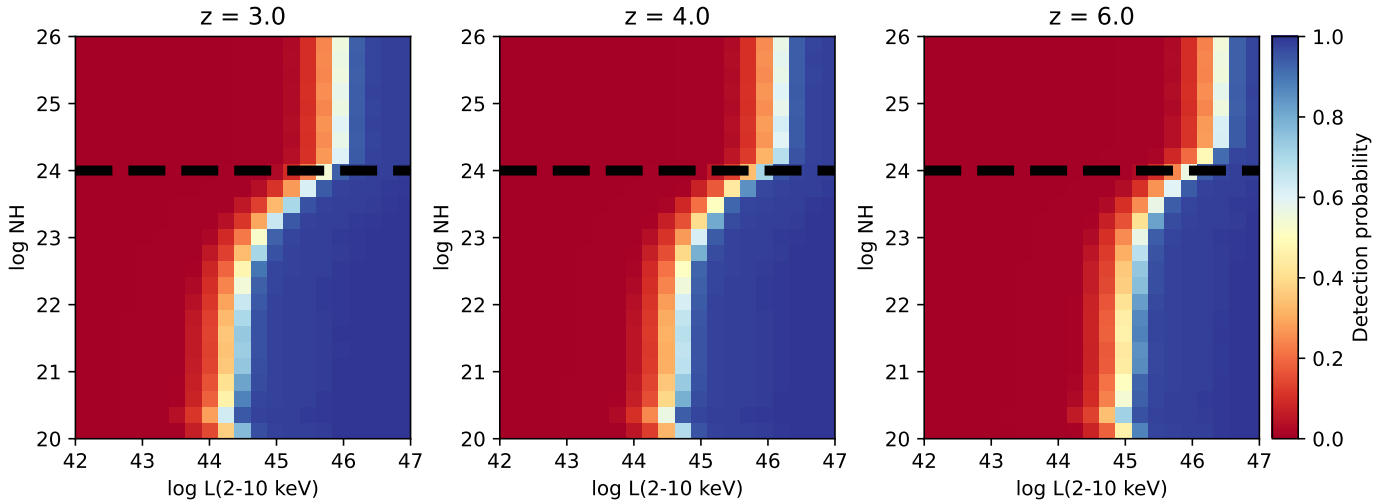


Fig. A.1: Sensitivity maps (Ω) for our survey. Each panel show the detection probability in the $\log L_X, \log N_H$ plane at three redshift values (3.0, 4.0, 6.0).

Table A.1: Prior limits and best-fitting values for the free parameters of the X-ray luminosity and absorption functions. Results are shown for both cases: using X-ray–only posteriors for the individual sources, and using posteriors updated with infrared (IR) information.

	Parameter	Prior limits	Best-fit value	
			X-ray	X-ray and IR
Luminosity function	$\log A$	[-5, -3]	$-4.25^{+0.10}_{-0.10}$	$-4.03^{+0.09}_{-0.10}$
	$\log L_*$	[42, 46]	$44.60^{+0.08}_{-0.07}$	$44.36^{+0.08}_{-0.07}$
	γ_1	[-2, 2]	$0.25^{+0.09}_{-0.09}$	$0.13^{+0.10}_{-0.10}$
	γ_2	[1, 6]	$2.35^{+0.17}_{-0.16}$	$2.16^{+0.13}_{-0.12}$
	$p_{\rm den}$	[-10, -3]	$-8.53^{+0.49}_{-0.47}$	$-8.32^{+0.47}_{-0.46}$
Absorption function	ε	[0, 10]	$2.841^{+0.37}_{-0.31}$	$2.14^{+0.29}_{-0.27}$
	$f_{\rm CTK,r}$	[0, 10]	$0.35^{+0.28}_{-0.25}$	< 0.32
	ψ_3	[0, 1]	$0.60^{+0.39}_{-0.25}$	$0.99^{+0.29}_{-0.98}$
	C	[-10, 10]	$-3.0^{+6.0}_{-6.8}$	$-2.4^{+8.9}_{-4.2}$
	a_2	[0, 15]	$10.6^{+3.6}_{-5.3}$	$12.1^{+2.7}_{-6.0}$

Notes. The normalisation, A, and the break luminosity, L_*, are given in units of Mpc^{-3} and $\mathrm{erg\,s}^{-1}$, respectively. The quoted best-fitting values and uncertainties correspond to the mode of the posterior distribution and the 1σ credible intervals around the mode.

To sample the posterior distribution of the model parameters, we used the nested-sampling Monte Carlo algorithm MLFriends (Buchner 2016; Buchner & Bauer 2017), implemented in the `UltraNest` package. Nested sampling enables simultaneous exploration of the posterior distribution and computation of the Bayesian evidence, which allows a direct comparison between alternative XLF models through Bayes factors. This approach also provides a rigorous treatment of the uncertainties in the X-ray spectral parameters and photometric redshifts of the individual sources included in the analysis.

We adopted flat (uniform or log-uniform) priors for all free parameters, spanning ranges broad enough to encompass the values reported in previous studies. Table A.1 lists the adopted prior limits for each parameter of the XLAF model.

Following the formulation of Loredo (2004), the likelihood of observing a given dataset can be expressed as the product of the probabilities of detecting each individual source multiplied by the probability of not detecting any additional sources. The corresponding log-likelihood, following Buchner et al. 2015, is:

$$\ln \mathscr{L} = -\lambda + \sum_i \ln \iiint P_i(L_X, z, N_H|\mathbf{\Theta}) \frac{dV}{dz} d\log N_H \, d\log L_X \, dz, \tag{A.8}$$

where λ represents the expected number of detected sources in a Poisson process for an XLF model with parameters $\mathbf{\Theta}$:

$$\lambda = \iiint \phi_{\rm abs}(L_X, z, N_H|\mathbf{\Theta}) \Omega(L_X, z, N_H) \frac{dV}{dz} d\log N_H \, d\log L_X \, dz, \tag{A.9}$$

and $\phi_{\rm abs} = \phi \times f_{\rm abs}$, where ϕ and $f_{\rm abs}$ are the luminosity and absorption functions defined above. $\Omega(L_X, z, N_H)$ is the survey sensitivity function, for which we adopted the values calculated by Pouliasis et al. (2024).

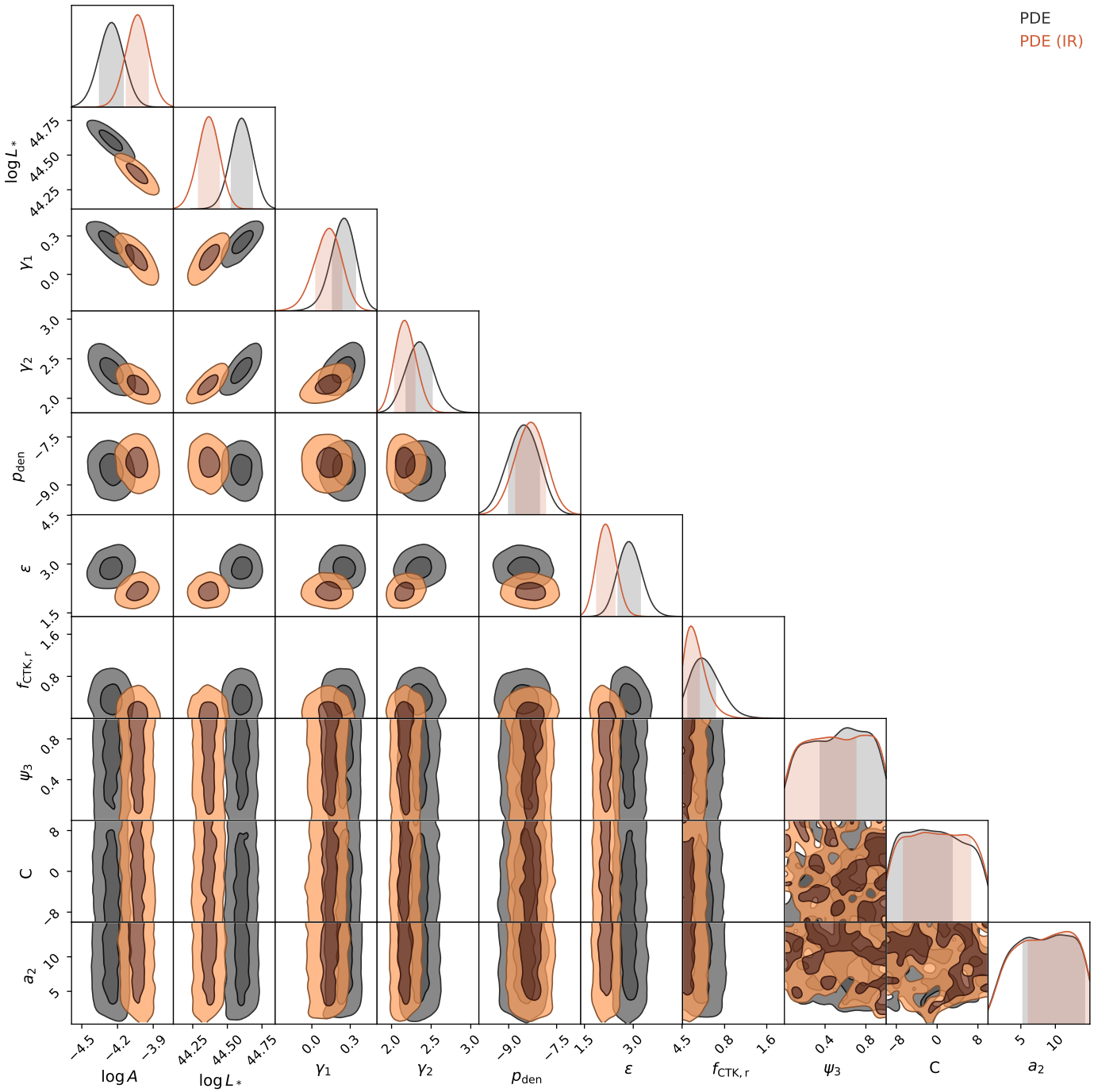


Fig. A.2: 1D and 2D marginal posterior distributions for the XLAF parameters. Black: X-ray only posteriors; red: posteriors updated with IR data.

The term P_i in Eq. A.8 is defined as:

$$P_i(L_X, z, N_H|\mathbf{\Theta}) = p(d_i|L_X, z, N_H)\ \phi_{abs}(L_X, z, N_H|\mathbf{\Theta})\ \Omega(L_X, z, N_H). \quad (A.10)$$

where $p(d_i|L_X, z, N_H)$ is the probability that source i has X-ray properties (L_X, z, N_H), given by the posterior distributions obtained from the Bayesian X-ray spectral fitting. Alternatively, the IR-updated posteriors discussed in Sect. 3.2 can be used here. The inclusion of Ω within this term accounts for the loss of information caused by differences between X-ray source detection and spectral fitting procedures (see Buchner et al. 2015, Appendix A, for a detailed discussion).

The integral in Eq. A.8 is evaluated using importance-sampling integration techniques (Kloek & van Dijk 1978; Press et al. 2007). The integration limits adopted for z, $\log L_X$, and $\log N_H$ are [3, 6], [42, 47], and [20, 26], respectively.

Our combined parametrisation of the luminosity and absorption functions includes ten free parameters. Table A.1 lists the best-fitting parameter values and their uncertainties for the assumed PDE model. Figure A.2 shows the one-dimensional (diagonal panels)

and two-dimensional marginal posterior distributions of the XLAF parameters. Results based on X-ray–only posteriors are shown in grey, while those incorporating IR-updated posteriors are shown in red. Most luminosity-function parameters remain consistent within 2σ between the two cases, whereas the inclusion of IR data shifts the absorption-related parameters ε and $f_{\mathrm{CTK},r}$ toward lower values. The parameters governing the redshift evolution of the absorption function (ψ_3, C, and a_2) remain poorly constrained, indicating that our dataset does not provide significant evidence for absorption-function evolution within the studied redshift range.

Appendix B: X-ray properties

This appendix presents, in Figs. B.1 and B.2, the X-ray cutouts and spectra for the ten CTK AGN candidates included in our sample. For each source, we show the *Chandra* or *XMM-Newton* images in the observed 0.5–2 and 2–7 keV bands, together with the corresponding X-ray spectrum and best-fitting model derived from the Bayesian spectral analysis. We also display the marginalised posterior distributions for three key parameters: N_{H}, L_{X} and z. For sources with spectroscopic redshifts, the z distribution is represented by a single vertical red line.

These figures illustrate the data quality and spectral characteristics of the selected CTK candidates, highlighting the range of absorption levels and luminosities found within the sample. They also provide a visual summary of the Bayesian modelling results, allowing a direct assessment of the uncertainties and degeneracies that affect the determination of N_{H} and L_{X} for individual sources.

Appendix C: Grid of models for CIGALE

In this appendix we present the modules and parameter values (see Table C.1) we used in `CIGALE` for the modelling of the SED of CTK objects.

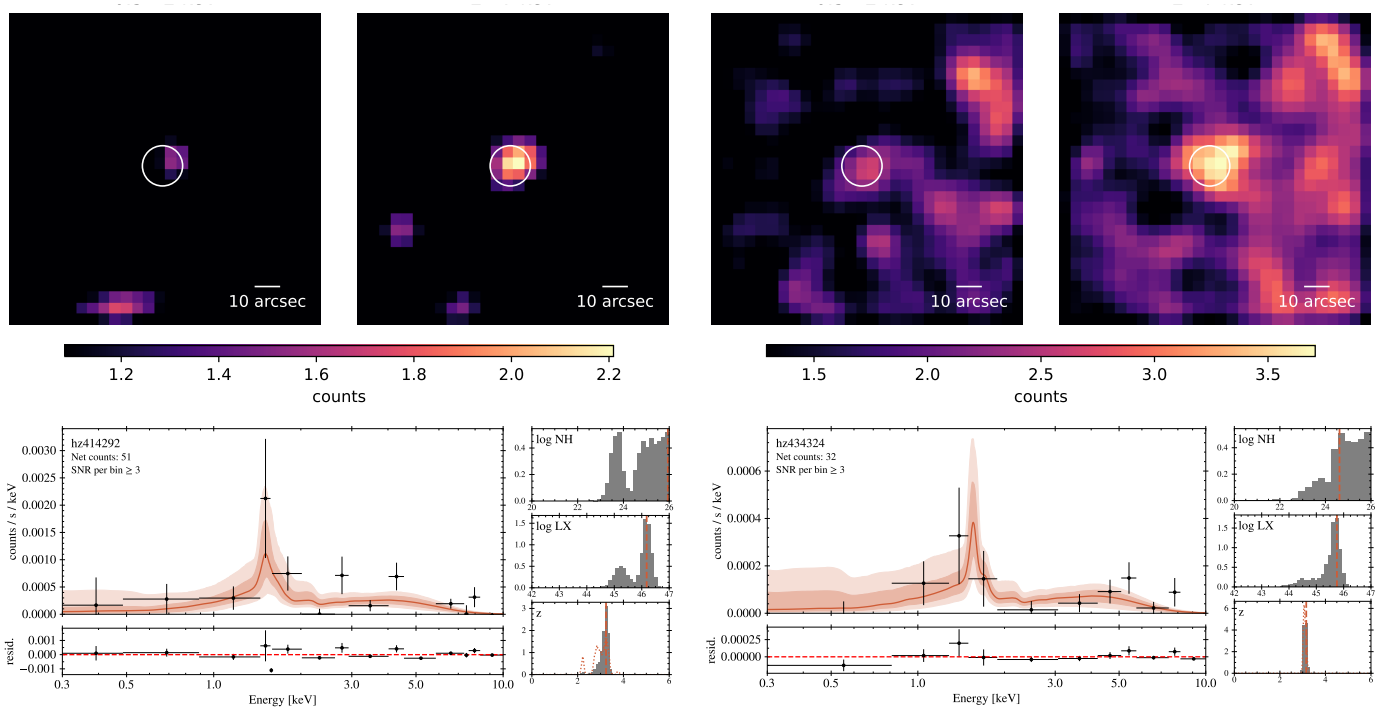


Fig. B.1: *XMM-Newton* cutouts and spectra for the selected CTK candidates. **Top:** Two arc-minutes *XMM-Newton*-EPIC cutouts in the 0.5-2 keV (left) and 2-7 keV (right) bands. **Bottom:** Co-added, background-subtracted *XMM-Newton*-EPIC spectrum. To improve visualization, the spectrum is binned. The red-shaded areas show the one- and two-sigma uncertainties for the best-fit source model (red, solid line). On the right column we plot the posterior distribution for $\log N_{\mathrm{H}}$ (top), $\log L_{\mathrm{X}}$ (middle), and redshift (bottom). The red, dashed lines show the mode of each distribution.

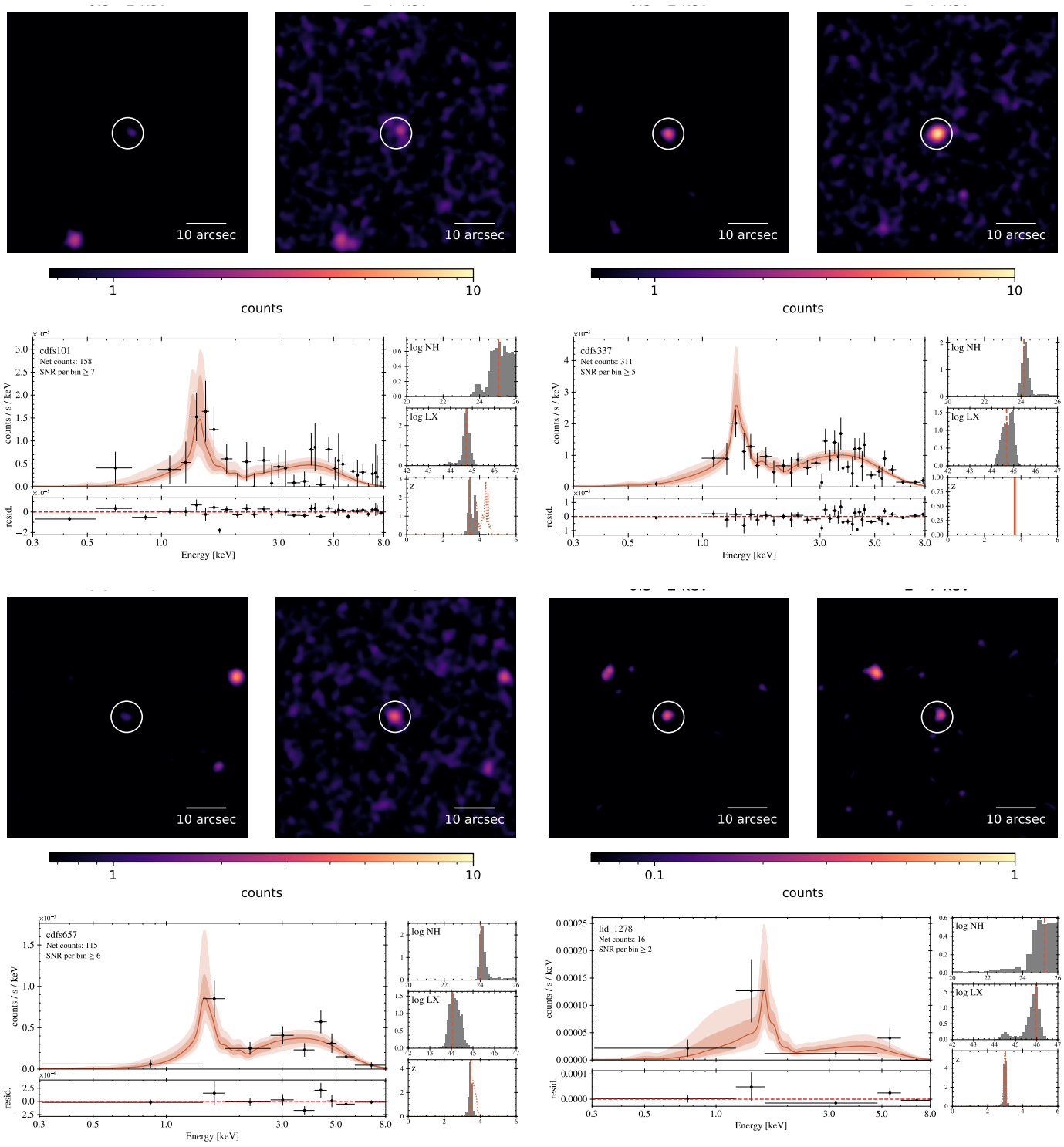


Fig. B.2: *Chandra* cutouts and spectra for the selected CTK candidates. **Top:** One arc-minutes *Chandra*-ACIS cutouts in the 0.5-2 keV (left) and 2-7 keV (right) bands. **Bottom:** Co-added, background-subtracted *Chandra*-ACIS spectrum. To improve visualization, the spectrum is binned. The red-shaded areas show the one- and two-sigma uncertainties for the best-fit source model (red, solid line). On the right column we plot the posterior distribution for $\log N_{\rm H}$ (top), $\log L_{\rm X}$ (middle), and redshift (bottom). The red, dashed lines show the mode of each distribution.

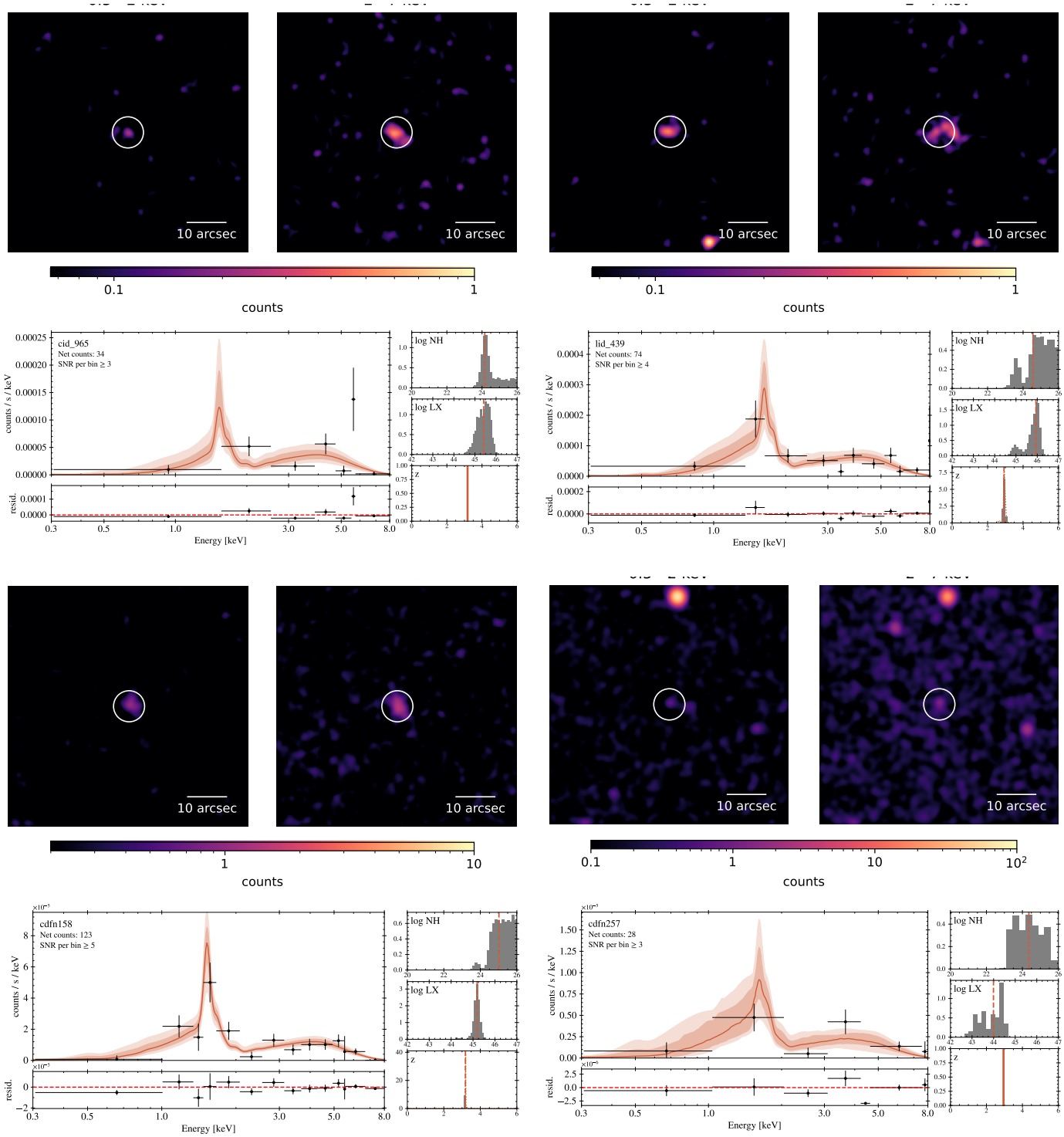


Fig. B.2: Continued.

Table C.1: CIGALE modules and parameter grid.

Module Parameter	Values	Description
sfhdelayed		Star formation history: delayed with exponential burst.
sfh.age_main	[500, 1000, 1500, 2000] Myr	Age of the main stellar population.
sfh.tau_main	[200, 500, 700, 1000, 2000] Myr	e-folding time of the main stellar population.
sfh.age_burst	[20] Myr	Age of the late burst population.
sfh.tau_burst	[50] Myr	e-folding time of the late burst population.
sfh.f_burst	[0.0, 0.005, 0.01, 0.015, 0.02, 0.05, 0.10]	Mass fraction of the late burst population.
bc03		Stellar synthesis population model (Bruzual & Charlot 2003).
stellar.imf	0	Salpeter's initial mass function (Salpeter 1955).
stellar.metallicity	[0.02] $Z_{\odot}$	Metallicity of the stellar population.
stellar.separation_age	[10] Myr	Age separation between old and young stellar populations.
nebular		Nebular emission.
nebular.logU	[-2.0]	Ionization parameter.
nebular.zgas	[0.014]	Gas metallicity.
nebular.ne	[100] cm^{-3}	Electron density.
nebular.f_esc	[0]	Fraction of Lyman continuum escaping the galaxy.
nebular.f_dust	[0]	Fraction of Lyman continuum absorbed by dust.
nebular.lines_width	[100] km s^{-1}	Line width (FWHM).
dustatt_modified_CF00		Dust attenuation: modified attenuation law (Charlot & Fall 2000).
attenuation.Av_ISM	[0.1, 0.2, 0.3, 0.4, 0.5, 0.6, 0.7, 0.8, 0.9, 1, 1.5, 2, 2.5, 3, 3.5, 4] mag	V-band attenuation in the ISM.
attenuation.mu	[0.44]	Attenuation ratio between the ISM and the birth clouds.
attenuation.slope_ISM	[-0.7]	Power law slope of the attenuation in the ISM.
attenuation.slope_BC	[-1.3]	Power law slope of the attenuation in the birth clouds.
dale2014		Dust emission from the galaxy.
dust.alpha	[1.0, 2.0, 3.0]	Slope for the dust emission law.
dust.fracAGN	[0]	Fraction of AGN luminosity set to zero. AGN emission is introduced by the SKIRTOR model.
skirtor2016		AGN model.
agn.t	[7, 9, 11]	Average edge-on optical depth at 9.7 μm.
agn.pl	[1.0]	Power-law exponent that sets the radial gradient of dust density.
agn.q	[1.0]	Index of the dust density gradient with polar angle.
agn.oa	[40] deg	Angle between the equatorial plane and the edge of the torus.
agn.R	[20]	Ratio of outer to inner radius of the torus (R_{out}/R_{in}).
agn.Mcl	[0.97]	Fraction of total dust mass inside clumps. 0.97 means 97% of total mass is inside the clumps and 3% in the interclump dust.
agn.i	[30, 50, 70, 90] deg	Viewing angle: i = [0, 90 - oa] (face-on, type 1 AGN); i = [90 - oa, 90] (edge-on, type 2 AGN).
agn.disk_type	1	Disc spectrum from Schartmann et al. (2005).
agn.delta	[-0.36]	Power-law of index δ modifying the optical slop of the disc. Negative values make the slope steeper where as positive values make it shallower.
agn.fracAGN	[0.0, 0.01, 0.1, 0.2, 0.3, 0.4, 0.5, 0.6, 0.7, 0.8, 0.9, 0.99]	Fraction of AGN IR luminosity to total IR luminosity (1 – 1000 μm).
agn.law	0	SMC extinction law for the polar dust.
agn.EBV	[0.0, 0.2, 0.4] mag	Extinction, E(B-V), in polar direction.
agn.emissivity	[1.6]	Emissivity index of the polar dust.
agn.temperature	[100] K	Temperature of the polar dust.